



Stochastic Micromechanical Damage Model for Porous Materials under Uniaxial Tension

Fengrui Rao¹; Longwen Tang, Ph.D.²; Yuhai Li³; Guanbao Ye⁴; Christian Hoover⁵; Zhen Zhang⁶; and Mathieu Bauchy⁷

Abstract: Despite the ubiquity of porous materials, their mechanical behaviors (e.g., fracture) remain only partially understood. Here, we propose a novel analytical stochastic micromechanical damage model to describe the fracture of porous materials subjected to uniaxial tension. This analytical model relies on parallel elastic and plastic elements to describe the nonlinear stress–strain curve of porous phases. We then develop a stochastic damage model to describe the propagation of randomly scattered voids or microflaws. This model allows us to identify the key influential features that govern the failure of porous materials. Finally, we demonstrate the accuracy of our model by validating its outcomes by a series of peridynamic simulations. **DOI: 10.1061/(ASCE)MT.1943-5533.0004146.** © 2022 American Society of Civil Engineers.

Author keywords: Porous materials; Peridynamic simulations; Micromechanical model; Stochastic damage model; Void structure.

Introduction

Porous materials are a class of materials with low density, unique pore structures, relatively high specific strength, and excellent thermal properties (Zhang et al. 2020). Typical porous materials used in engineering fields are rocks, concretes, ceramics, and so on (Chen et al. 2019; Fakhimi and Alavi Gharahbagh 2011; Falliano et al. 2018; Nikonam et al. 2020). Without a doubt, the most widely used porous material in infrastructure is concrete (Huang et al. 2017; Tikalsky et al. 2004; Yang et al. 2014; Yue-Dong and Jian 2011). Indeed, concrete exhibits a good balance between weight and

¹Ph.D. Candidate, Key Laboratory of Geotechnical and Underground Engineering of Ministry of Education, Dept. of Geotechnical Engineering, Tongji Univ., Shanghai 200092, China; Physics of AmoRphous and Inorganic Solids Laboratory, Dept. of Civil and Environmental Engineering, Univ. of California, Los Angeles, CA 90095. Email: 704819763@qq.com

²Physics of AmoRphous and Inorganic Solids Laboratory, Dept. of Civil and Environmental Engineering, Univ. of California, Los Angeles, CA 90095. ORCID: https://orcid.org/0000-0001-7809-8720. Email: whutang@ucla.edu

³Ph.D. Candidate, Physics of AmoRphous and Inorganic Solids Laboratory, Dept. of Civil and Environmental Engineering, Univ. of California, Los Angeles, CA 90095. Email: yuhaili@g.ucla.edu

⁴Professor, Key Laboratory of Geotechnical and Underground Engineering of Ministry of Education, Dept. of Geotechnical Engineering, Tongji Univ., Shanghai 200092, China. Email: guanbaoye@gmail.com

⁵Assistant Professor, School of Sustainable Engineering and the Built Environment, Arizona State Univ., Tempe, AZ 85287. Email: christian.hoover@asu.edu

⁶Associate Professor, Key Laboratory of Geotechnical and Underground Engineering of Ministry of Education, Dept. of Geotechnical Engineering, Tongji Univ., Shanghai 200092, China. Email: zhenzhang@tongji.edu.cn

⁷Associate Professor, Physics of AmoRphous and Inorganic Solids Laboratory, Dept. of Civil and Environmental Engineering, Univ. of California, Los Angeles, CA 90095 (corresponding author). ORCID: https://orcid.org/0000-0003-4600-0631. Email: bauchy@ucla.edu

Note. This manuscript was submitted on March 1, 2021; approved on August 13, 2021; published online on January 20, 2022. Discussion period open until June 20, 2022; separate discussions must be submitted for individual papers. This paper is part of the *Journal of Materials in Civil Engineering*, © ASCE, ISSN 0899-1561.

strength and can both be cast in place or precast (Mydin and Wang 2012; Hamad 2014; Amran et al. 2015). Many current investigations of porous materials have focused on elucidating the unique mechanical properties affected by attributes of porosity, such as pore size and connectivity (Hilal et al. 2015; Nguyen et al. 2018). Advanced apparatus like optical microscopy, mercury intrusion porosimetry (MIP), scanning electron microscopy (SEM), and X-ray computerized tomography (X-CT) are commonly used to probe the features of the pore structure, such as pore size distributions, adsorption and desorption isotherms, and pore connectivity (Chung et al. 2017; Hou et al. 2019; Nguyen et al. 2017). Data collected from these tests have enabled a better understanding of how the pore structure affects properties critical for design, such as the compressive strength (Nambiar and Ramamurthy 2007; Yu et al. 2011; Wei et al. 2013; Hilal et al. 2015; Hou et al. 2019). In general, the relationships between porosity and compressive strength, elastic modulus, or stiffness are known for concrete and cementitious materials (Amran et al. 2015; Hoover and Ulm 2015; Kearsley and Wainwright 2001; Liu 1997; Nikonam et al. 2020; Sadowski and Samborski 2003). However, these properties do not fully describe the mechanical behavior of porous materials (e.g., as captured by their stress-strain curve). In particular, porous materials tend to be very weak in tension. Therefore, it is important to understand and predict the whole stress-strain response of porous materials under tensile stress. Traditionally, the direct tensile strength of porous materials is very difficult to measure due to complications with load eccentricity and nonuniform stress or strain fields and stress concentrations, leading to a failure mode that is different than a uniform stress field reaching maximum threshold strength (van Mier and van Vliet 2002). Rather, the tensile stress is usually calculated from the so-called Brazilian split cylinder tests or single-edged notched fracture specimens with a preexisting deep notch (Tang et al. 2018; Zhao et al. 2020).

In porous materials, the location and size of microcracks and voids—formed both during the casting process and as a consequence of damage initiation and propagation during their lifetime—is highly random (Zhang and Jivkov 2014). This makes it difficult to create samples with tailored or designed void structures that are necessary for rigorous experimental analyses. This makes numerical simulation an effective and practical alternative.

Numerical simulations describing the mechanical behavior of porous materials have attracted great interest over the last decades. Many popular models are based on the finite-element method (FEM) (Chung et al. 2017; Kuna et al. 2020; Mugahed Amran et al. 2016), extended finite-element method (XFEM) (Ferretti et al. 2015; Kozlowski et al. 2016; Rezanezhad et al. 2019), or discrete element method (DEM) (Fakhimi and Alavi Gharahbagh 2011; Nguyen et al. 2017, 2019). In the FEM, the mechanics of fracture is mainly captured by smeared crack approaches, nonlocal models coupled with isotropic or anisotropic damage models, local tensorial formulations of smeared cracking, microplane models, and so on. For these methods, an additional preprocessing technique is required at the discontinuous part (Huang et al. 2015; Liu et al. 2020; Wang et al. 2016). When modeling fracture in XFEM, a crack is introduced within the mesh without refinement, and an external criterion is needed to predict crack growth (Unger et al. 2007). However, the complex enrichment functions needed to use XFEM demand significant computational expense and complicate implementation. With the assumption that discrete elements interact by means of contact forces, DEM provides a powerful tool for fracture simulation at the meso scale. However, characterizing the parameters that define interactions among various phases in a heterogeneous material demands some significant efforts (Yaghoobi et al. 2017). Here, as an alternative route, we adopt peridynamics. Peridynamics is a nonlocal theory of the mechanics of solid deformations. It was originated by Silling (2000) to mathematically describe the mechanics of continuous and discontinuous media. This is achieved by replacing the partial spatial derivatives in the governing equations with integral formulations. In peridynamics, the material domain is discretized into points with a finite volume. Each materials point x interacts with the other points x' that are located within a specific region, which is often assumed to be a sphere centered around x with a radius ζ ; this radius is known as the "horizon" and is typically three times the particle size. This makes it possible to model damage in materials without the need for complex numerical treatments at discontinuities and crack tips (Behzadinasab and Foster 2020; Chen et al. 2019; Kilic et al. 2009). Therefore, peridynamics is a convenient and promising tool to simulate the complete fracture process of porous materials, such as foamed concrete (Yaghoobi et al. 2017), ceramics (Bazazzadeh et al. 2020; Mitts et al. 2020), porous rocks (Rabczuk and Ren 2017; Zhou et al. 2020), and so on.

Although numerical simulations offer a powerful tool to predict the stress-strain curves of porous phases upon uniaxial tension, their "black-box" nature makes it challenging to identify the key physics governing the failure of porous phases. In parallel to numerical simulations, only a few analytical theoretical models describing the failure of porous materials have been proposed. Recently, two main approaches have been widely adopted for the modeling of porous materials: (1) the continuum damage model (CDM); and (2) micromechanical models. On the one hand, based on irreversible thermodynamics, the CDM provides a powerful method for constructing constitutive models. Many endeavors have helped to improve the CDM framework to elucidate the mechanism of damage and failure (Faria et al. 1998; He et al. 2015; Ju 1989; Wu et al. 2006). Although the CDM offers a sound theoretical framework, damage cannot be expressed theoretically therein. It must be expressed using empirically calibrated functions, in which several parameters without clear physical meaning are required to be determined (Li and Ren 2009). On the other hand, micromechanical models are physically well grounded and take into account the evolution and propagation of random microflaws in the solids by introducing the parallel jointed microelement and damage coupling (Li and Ren 2009). Micromechanical models can also capture stochastic damage evolution (Li and Guo 2020) and provide deep insight into the physics behind the fracture process of porous materials.

This paper aims to provide a novel stochastic micromechanical damage model describing the behavior of porous materials under uniaxial tension. The model system consists of a brittle matrix filled with randomly scattered voids. To assess the effects of porosity and void structure, we adopted peridynamic simulations to compute the entire stress–strain response under uniaxial tension. The peridynamic simulations were then used to inform and validate a micromechanical model that embedded a stochastic damage model—which aimed to analytically describe the mechanical response of porous phases. The present model not only properly describes the nonlinear mechanical response of porous materials but also captures the effect of the heterogeneous structure of porous material. The overall harmony between theoretical and numerical results supports the ability of our new model to offer a realistic description of the failure of porous materials.

Method

Peridynamic Theory

In peridynamics, the material domain is discretized into particles within a finite volume. A particle located at position \mathbf{x} interacts with its surrounding particles \mathbf{x}' within an area of influence called a horizon. For convenience, the horizon is assumed to be a sphere centered on \mathbf{x} with a radius ζ . The relative position between two interacting particles is defined as a bond $\xi = \mathbf{x}' - \mathbf{x}$. The relative displacement between two particles is defined as $\eta = \mathbf{u}(\mathbf{x}',t) - \mathbf{u}(\mathbf{x},t)$, where \mathbf{u} is the displacement vector field. When the stretching η exceeds a critical value, the bond between two particles breaks down, which means the interaction between these particles ceases to exist. This breaking is irreversible.

The peridynamic equation of motion at particle \mathbf{x} and time t is given by

$$\rho(\mathbf{x})\ddot{\mathbf{u}}(\mathbf{x},t) = \int_{\zeta} [\mathbf{T}(\mathbf{x},t)\langle \mathbf{x}' - \mathbf{x} \rangle - \mathbf{T}(\mathbf{x}',t)\langle \mathbf{x} - \mathbf{x}' \rangle] dV_{\mathbf{x}'} + \mathbf{b}(\mathbf{x},t)$$
(1)

where ρ = local density; $\mathbf{b}(\mathbf{x},t)$ = external body force density; $dV_{\mathbf{x}'}$ = infinitesimal volume around \mathbf{x}' ; and \mathbf{T} = force vector state that describes the interaction force between points, which depends on the constitutive model used in the simulation. For ordinary state-based peridynamics models, the constitutive model can be expressed as

$$\mathbf{T} = \begin{cases} \mathbf{C} \frac{\xi + \eta}{\|\xi + \eta\|} & \|\xi + \eta\| \neq 0\\ 0 & \|\xi + \eta\| = 0 \end{cases}$$
 (2)

where C = scalar state, which is determined by the elastic parameters of the material.

In this paper, we adopt the state-based linear peridynamic solid (LPS) constitutive model (Silling et al. 2007). This model assumes that the force is proportional to the deformation following a linear elastic response until the fracture point is reached. The state-based LPS constitutive model uses as inputs arbitrary bulk and shear moduli values, which, in turn, dictate the value of Poisson's ratio. The scalar state is given by

$$\mathbf{C} = \frac{3K\theta}{m}\omega\mathbf{x} + \frac{15S}{m}\omega\mathbf{e}^{\mathbf{d}} \tag{3}$$

where K and S = bulk and shear moduli respectively; m = weight volume; θ = dilatation, ω = influence function; and $\mathbf{e^d}$ = deviatoric part of the extension scalar state \mathbf{e} .

The propagation of cracks in peridynamics is described by the breaking of bonds, characterized by a critical bond stretching distance, S_c , which is dependent on the constitutive model. For a three-dimensional linear elastic model, S_c is expressed as

$$S_c = \sqrt{\frac{G_f}{[3S + (\frac{3}{4})^4 (K - \frac{5S}{3})]\zeta}}$$
 (4)

where G_f = fracture energy of the material.

Stochastic Micromechanical Damage Model

Here, we model the mechanical behavior of porous phases under uniaxial tension as a series of individual elements jointed in parallel [Fig. 1(a)]. The elements are linked with rigid bars on the ends so that they undergo uniform deformations during the loading process. This is typically referred to as a "bundle" model (Li and Ren 2009). If there are many elements in series and in parallel, this is referred to as a "bundle and chain" model (Li and Ren 2009). A pair of spring and damper in parallel is referred to as a Kelvin–Voigt element, whereas a spring and damper in series is referred to as a Maxwell element. The model has two scales: (1) meso scale; and (2) macro or structural scale. An individual element represents

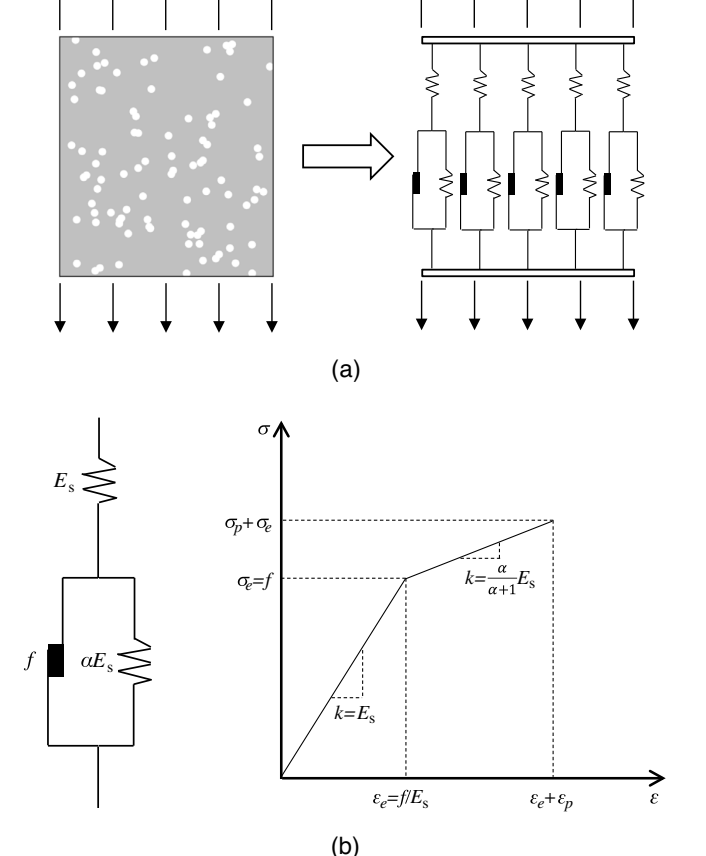


Fig. 1. Idealized model describing the mechanics of porous materials subjected to uniaxial tension: (a) parallel element model, wherein the mechanical behavior of the material is described in terms of spring and damper in parallel and in series; and (b) stress—strain relationship associated with an individual element.

the meso-scale homogenized properties of the material, whereas the element system describes the macroscopic response. Therefore, complex macromaterial behaviors can be obtained based on the parallel system, wherein the individual element is endowed with simple material properties.

Fig. 1(b) shows the stress–strain relationship of a microelement expressed by Eq. (5)

$$\sigma = \begin{cases} E_s \varepsilon_e \text{ when } \varepsilon \leq \varepsilon_e, & \text{where } \varepsilon_e = f/E_s \\ f + \alpha E_s(\varepsilon - \varepsilon_e)/(\alpha + 1) & \text{when } \varepsilon > \varepsilon_e \end{cases}$$
 (5)

The elastic response of materials is represented by a purely elastic spring element with the modulus of E_s . The strain that initiates the inelastic fracture behavior is randomly generated. The spring element is in series with a parallel combination of a spring (with a modulus αE_s) and damper (with a threshold f) to capture the plastic response. Even though, at the particle level, the peridynamic simulation relies on a purely linear–elastic constitutive model, the simulated system may still exhibit some level of plasticity at the macro scale, for example, via crack deflection, branching, or arresting. To phenomenally describe the resulting stress–strain relationship, we introduced the so called "damping element." This element prevents the parallel spring from stretching until a threshold force f is reached. The fracture strain is assumed to be identical in the two springs that belong to the same bundle, to prevent the infinite plastic flow in this model.

In this micromechanical model, the propagation of cracks inside porous material was simulated by the sequential fracture of individual elements throughout the entire loading process (Fig. 2). Assuming that the total number of individual elements is N, the spatial coordinate of the ith element is i/N, and the random fracture strain of ith element is \bar{i} (i = 1, 2, ... N).

During the tension test, the external load was supported by the undamaged part of the material. The equation of the stress– strain relationship of the porous material can then be expressed as [50, 51]

$$\sigma = [1 - d(\varepsilon)]E(\varepsilon)\varepsilon \tag{6}$$

where $d(\varepsilon)$ = damage; and $E(\varepsilon)$ = strain-dependent modulus of the macroscopic system (i.e., including porosity effects). The classic definition of damage (Rabotnov 1969) is

$$d = 1 - A_e/A \tag{7}$$

where A= cross-sectional area; and $A_e=$ undamaged area. Accordingly, the damage in the micromechanical model can be expressed as

$$d(\varepsilon) = \frac{1}{N} \sum_{i=1}^{N} H(\varepsilon - \Delta_i)$$
 (8a)

where H(x) = Heaviside function

$$H(x) = \begin{cases} 0 & x < 0 \\ 1 & x > 0 \end{cases} \tag{8b}$$

When N approaches infinity, one gets

$$d(\varepsilon) = \int_{0}^{1} H(\varepsilon - \Delta(x)) dx \tag{9}$$

where x = spatial coordinate of the element (i.e., ith element); and $\Delta(x)$ = fracture strain at x, $\Delta(x) = \Delta_i$. Therefore, the equation

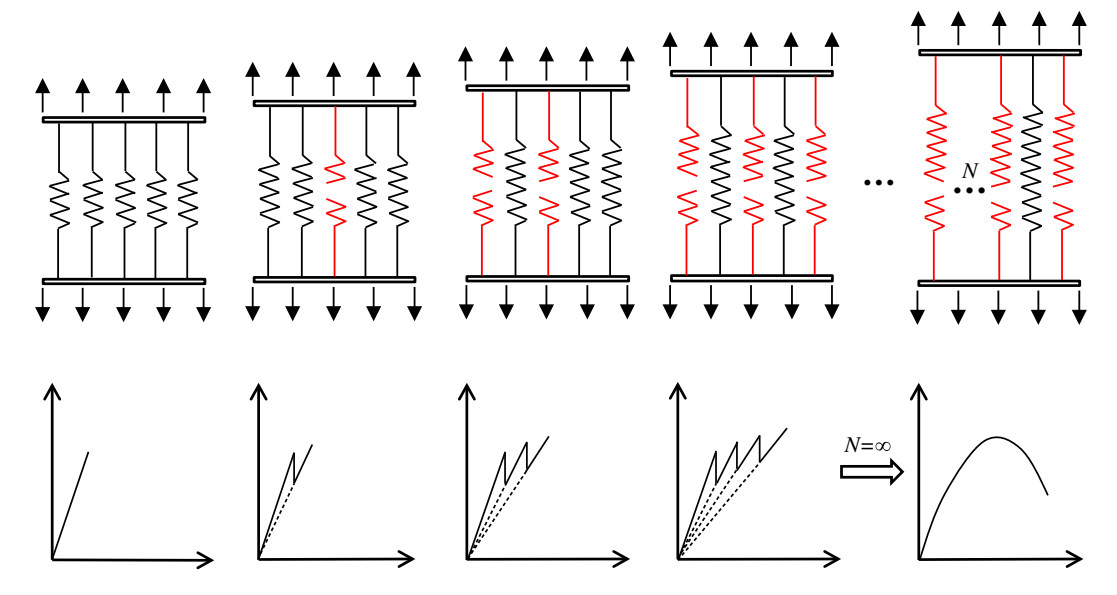


Fig. 2. Schematic of the stress-strain response yielded by the present micromechanical damage model for different numbers of elements.

of the stress-strain relationship of the porous material can be expressed as

$$\sigma = \int_0^1 H(\Delta(x) - \varepsilon) \cdot E(\varepsilon)\varepsilon dx = [1 - d(\varepsilon)]E(\varepsilon)\varepsilon \tag{10}$$

As mentioned previously, $\Delta(x)$ is a random value. Let us assume that $\Delta(x)$ is a homogenous random field with the first-order density functions

$$f(\Delta; x) = f(\Delta) \tag{11}$$

Setting $\varphi(x)=H(\varepsilon-\Delta(x)),\ \varphi(x)$ follows the $(0,\ 1)$ distribution, that is

$$P[\varphi(x) = 1] = P[(\varepsilon - \Delta(x)) \ge 0] = \int_0^\varepsilon f(\Delta) d\Delta = F(\varepsilon) \quad (12)$$

$$P[\varphi(x) = 0] = 1 - F(\varepsilon) \tag{13}$$

As such, the expected value of damage can be expressed as

$$\mu = \mathbf{E}[\varphi(x)] = F(\varepsilon) \tag{14}$$

where $\mathrm{E}[\varphi(x)]=$ expectation operator. Accordingly, Eq. (10) can be reformulated as

$$\sigma = \mathbf{E}[\sigma] = (1 - \mu)E(\varepsilon)\varepsilon \tag{15}$$

In this paper, the randomness of the damage evolution in porous materials is assumed to follow a lognormal distribution, which is commonly adopted in the context of porous rocks, concrete-like material, ceramics, and other porous materials (Arson and Pereira 2013; Kandarpa et al. 1996; Li and Ren 2009; Lu et al. 2013; Maiti et al. 2005; Ozaki et al. 2018; Silling et al. 2007). Following $\ln \Delta(x) \sim N(\lambda, \delta^2)$, one gets

$$\mu = F(\varepsilon) = \phi \left[\frac{\ln \varepsilon - \lambda}{\delta} \right] = \phi(\alpha) \tag{16}$$

where $\phi(\alpha)$ = cumulative distribution function of a standard normal distribution.

Model Development and Validation

Numerical Model Development for Porous Materials

The target porous material system was modeled as a composite system with a distinct set of unit cells. Within the simulation region, the cells were assigned to be a solid or void, wherein the number of void cells was constrained by the desired final porosity. All models had a size of 26 × 26 unit cells. Herein, we simulated single-edge notched tension specimens with an initial notch with length equal to 5 unit cells (a relative depth of 19%, see Fig. 3). Previous studies have shown that peridynamic frameworks can properly describe the fracture behavior of composite systems when the grid spacing is smaller than a tenth of the inclusion diameter (Agwai et al. 2011; Yaghoobi et al. 2017). In this study, the unit cell was fixed to 10 grid spacing, and a lattice spacing of 15 nm was found to yield a convergence in the computed stress-strain curve. The size of a pore cell (150 nm) was close to the typical size of capillary pores in cement pastes (Dong et al. 2017). A system size of 26×26 pixels (i.e., 260×260 lattice points) was adopted for computational efficiency purposes. Although the size of the representative element volume would be expected to increase upon increasing porosity, here, the representative volume element was kept constant to ensure a meaningful comparison between samples featuring varying porosities. The thickness of the whole system was fixed at 10 lattice spacing, which is large enough for the elastic response of the system to convergence. The horizon was fixed as three times the grid spacing. The solid matrix was considered brittle, and the mechanical properties of cement paste phase were used, that is, Young's modulus E = 25 GPa (Constantinides and Ulm 2004; Yaghoobi et al. 2017; Youssef et al. 2018), fracture energy $G_f = 1.75 \text{ J/m}^2$ (Bauchy et al. 2015), and Poisson's ratio v = 0.2.

Simulation of Uniaxial Tensile Test

A uniaxial tensile test was conducted by subjecting the simulated sample to a constant displacement rate (velocity) to the top and bottom boundaries of the model. A boundary thickness of three grid

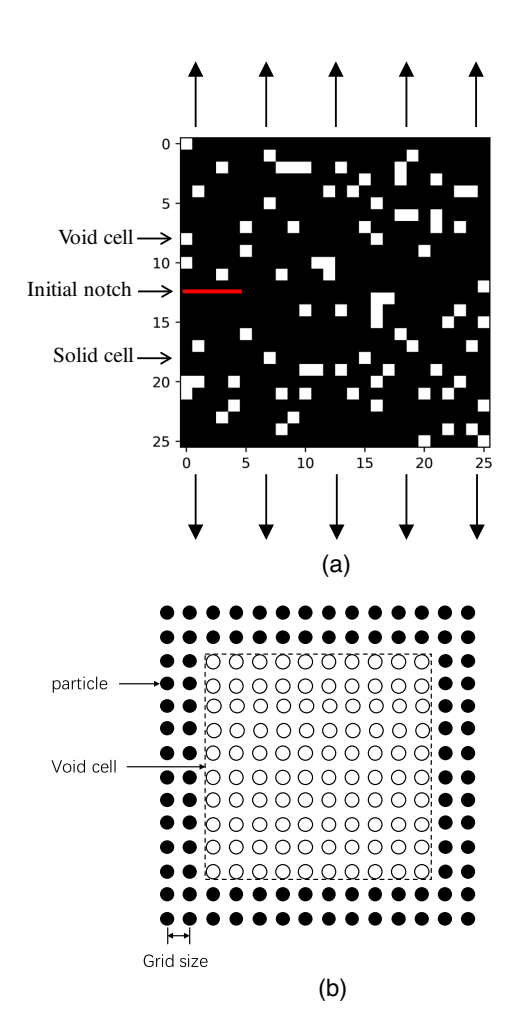


Fig. 3. Schematic of the porous material model used herein: (a) white and black pixels denote void cells (pores) and solid cell (matrix), respectively. The numbers of pixels are marked in the x-direction and y-direction. The arrows denote the direction of the imposed tension. The line indicates the position of the initial notch that is used to induce a stress concentration; and (b) schematic illustrating the discretization of each unit cell into 10×10 particles.

spacings—which was large enough to account for all interactions between boundary and inner part—was selected to avoid any spurious effect arising from nonlocal interactions close to the free surface (Madenci and Oterkus 2014). The integration timestep was decided based on a von Neumann stability analysis to guarantee the stability of the simulation (Silling and Askari 2005). We adopted the open-source Peridigm package to run all the simulations (Tang et al. 2018).

The effect of the strain rate on the fracture behavior of pure brittle materials needed to be assessed. Fig. 4 shows the computed stress–strain curve and fracture energy for the model with no voids. The fracture energy is calculated by integrating the stress– strain curve

$$G_f = c \int \sigma_z dl_z \tag{17}$$

where c depends on the area of the notch and on the direction of crack propagation. In the simulation model shown in Fig. 3, c was calculated as c = 26/(26-5) = 1.24, where 26 and 5 are the lengths of the system and notch, respectively (in units of number of unit cells). The values σ_z and l_z are the stress and displacement in the loading direction (z-axis), respectively.

As expected, we observe from Fig. 4(a) that the stress linearly increased with strain until the fracture point was reached. The elastic regime remained unaffected by the strain rate. However, when the strain rate exceeded 2×10^5 s⁻¹, the model started to show some ductility after the fracture point was reached, thereby resulting in an increase in the fracture energy [Fig. 4(b)]. A similar phenomenon was also reported by Tang et al. (2018) in the study of phase-separated glasses. This can be explained by an inertia effect; that is, when the strain rate increases, the inertia around the crack tip grows and leads to crack branching or a "zig-zag" crack path (Tang et al. 2018). Similarly, the fracture energy converges when the strain rate becomes equal to or lower than 10⁵ s⁻¹. Because the simulation model is relatively small, the inertia effect can be neglected in this range of strain rate. The same convergence can also be observed in models exhibiting different porosities. Accordingly, a strain rate of 10⁵ s⁻¹ was adopted in this study to balance computational efficiency and accuracy.

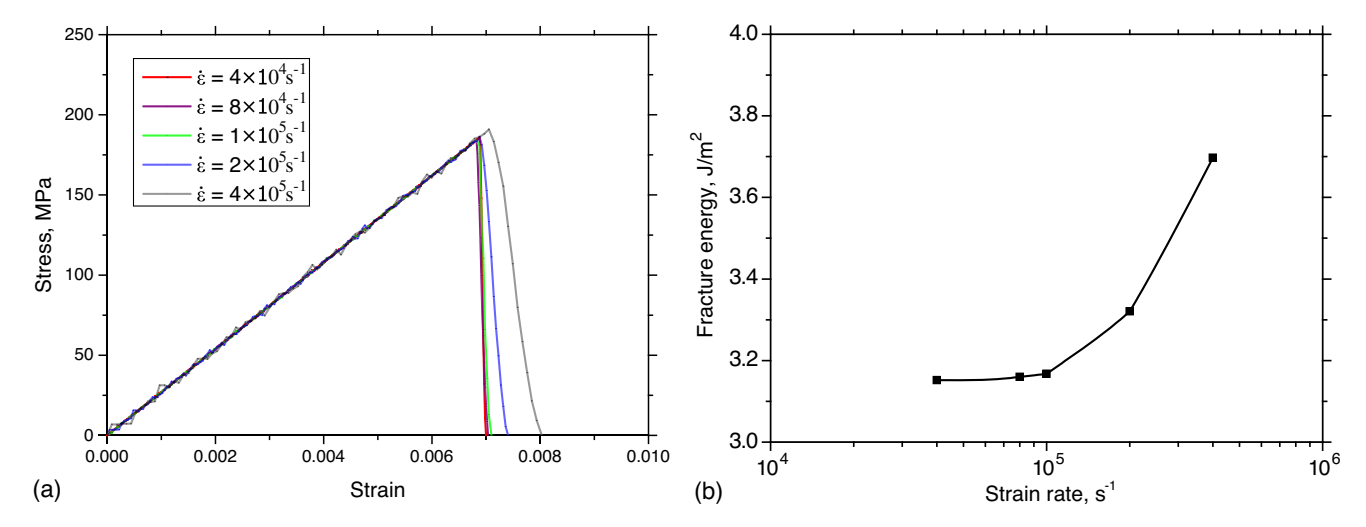


Fig. 4. Simulation results obtained for the model without voids: (a) computed stress–strain curve for varying strain rates; and (b) associated fracture energy [calculated from Eq. (17)] as a function of the strain rate.

Table 1. Parameters adopted herein for the numerical simulations

			Young's		Fracture
		Density	modulus	Poisson's	energy
Case	Porosity	(kg/m^3)	(GPa)	ratio	(J/m^2)
Rezanezhad et al. (2019)	_	2,700	70.6	0.25	38.5
Fakhimi and Alavi	16.5%	2,500	0.09	0.20	11.6
Gharahbagh (2011)					

Validation of the Peridynamics Method

Peridynamics has been widely adopted to explore the fracture mechanisms of porous materials (Chen et al. 2019; Katiyar et al. 2020; Li and Guo 2020; Yaghoobi et al. 2017). Yaghoobi et al. (2017) studied the fracture behavior of foamed concrete under uniaxial tension using peridynamics. The results matched well with FEM simulations results while demanding much less computational cost. Chen et al. (2019) explored the dynamic properties and elastic moduli of porous glasses using a peridynamics model and obtained a good match with experimental results. To further verify the reliability and applicability of the peridynamics method in simulating uniaxial mechanical behavior, the results of Rezanezhad et al. (2019) and Fakhimi and Alavi Gharahbagh (2011) are herein used as references. Rezanezhad et al. (2019) investigated the effects of pore and crack locations during crack propagation using XFEM. The properties of materials used in the models are given in Table 1, and the configuration of the model is shown in Fig. 5(a). The same model was rebuilt in Peridigm with lattice spacing of 0.5 mm. The comparison of the results from XFEM and peridynamics is shown in Figs. 5(b and c). It can be concluded that, for a model with one pore, the displacement-force curve computed from peridynamics matches well with that offered by XFEM. Similarly, for a model with two pores, the peridynamic model can properly describe the propagation and deflection of cracks. Fakhimi and Alavi Gharahbagh (2011) investigated the effect of pore size and pore distribution on the mechanical behavior of sandstone with a porosity of 16.5%. In this study, a two-dimensional DEM method and twodimensional model were involved to get the stress-strain response of porous rock under uniaxial tension. The properties of materials used in the models are given as Table 1, and the same model was here rebuilt in Peridigm with a lattice spacing of 0.5 mm. The comparison of the results from DEM and peridynamics is shown in Fig. 6. It can be concluded that, for a complicated system with relatively high porosity, the peridynamics method can properly describe the stress-strain response of the model.

Results and Discussion

Numerical Results

Having established the ability of the peridynamic simulation to offer a realistic description of the failure of porous phases, we now explore the effect of porosity. To this end, a series of models exhibiting porosity ranging from 3% to 30% with 3% increments was simulated. Even though the porosity range is a lower-bound range for calcium–silicate–hydrate (C–S–H) gel, we aim to derive more generic insights into the relationship between porosity and mechanical behavior of porous solids. For each value of porosity, 100 samples with randomly scattered voids were generated. This led to 1,000 samples in total. For convenience of later discussion, Fig. 7 defines some terms used herein to describe and interpret the stress–strain curve. Fig. 8 shows part of the stress–strain curve of different porosity groups. As expected, the modulus and peak stress decreased with increasing porosity. An increase in the ultimate

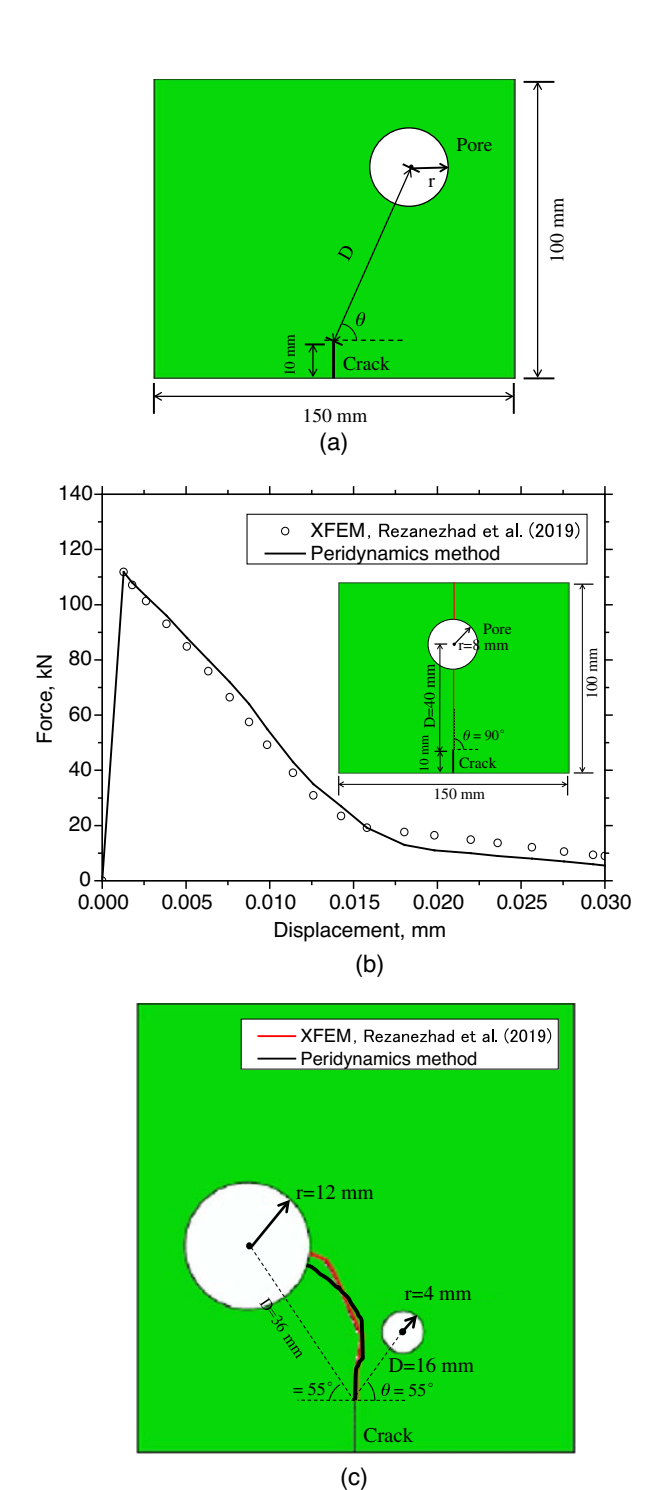


Fig. 5. Comparison of the peridynamic method with XFEM reference results: (a) schematic illustrating the size and position of a pore with respect to an initial crack; (b) displacement–force curve computed by peridynamics for the one-pore model shown in the inset. The results are compared with those obtained by XFEM simulations for the same system (Rezanezhad et al. 2019); and (c) predicted crack propagation path obtained by peridynamics for a two-pore model. The results are compared with reference XFEM simulations for the same system (Rezanezhad et al. 2019).

strain was also observed as porosity increased. This arises from both the fact that (1) cracks are locally attracted toward the soft regions formed by densely distributed voids, thereby inducing strong crack deflections that postpone the ductile stage of the model, and

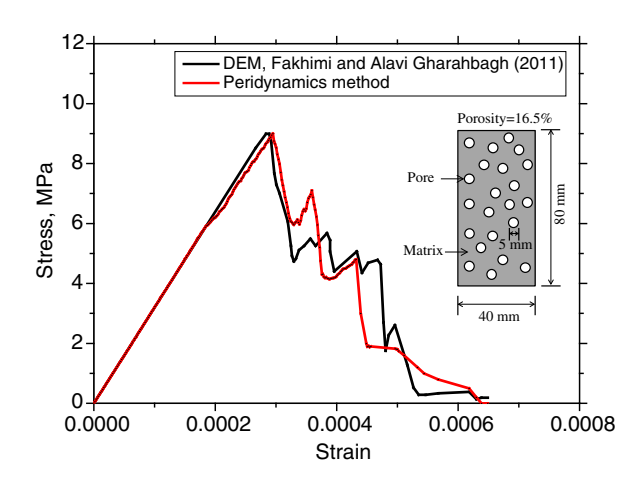


Fig. 6. Stress–strain curve computed by peridynamics for the porous phase shown in the inset. The results are compared with those obtained by DEM simulations for the same system (Fakhimi and Alavi Gharahbagh 2011).

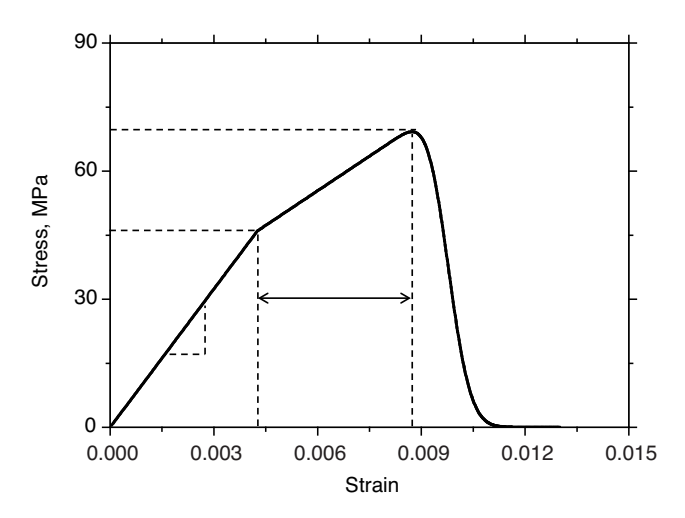


Fig. 7. Schematic illustrating the typical features of a stress–strain curve that are used herein to describe the mechanical response of a porous phase subjected to uniaxial tension.

(2) microcracks tend to nucleate in high-porosity regions due to local stress concentrations around a pore. Because mechanical behavior tends to become more ductile upon increasing porosity, models with different porosities were here divided into two groups for further analysis: (1) a low-porosity group, which contained models with porosity from 3% to 15%; and (2) a high-porosity group, which contained models with porosity from 18% to 30%. In these two cases, the obtained stress–strain curves tended to show (1) fairly brittle behavior; and (2) a more obvious yielding regime, respectively.

Some significant heterogeneity was observed in each porosity group. For illustration purposes, a statistical analysis of the data is shown in Fig. 9. The data shown in the Fig. 9 were obtained from the analysis of 100 samples in each group—a number of samples that is large enough to ensure a convergence of the statistical distribution [Fig. 9(f)]. The max values of modulus and yield stress in each group were linearly fitted [see insert in Figs. 9(a and d)]. In general, the modulus, peak stress, yield strain, and yield stress decreased with the increase of porosity at all percentile values. In groups of low porosity, such as 3%–9%, the scatter in the modulus was generally less than 10%, whereas the scatter grew noticeably

with the increase of porosity [Fig. 9(a)]. As for peak stress, a relatively small variance in percentile 25%–75% was observed in samples of two extreme porosities, 3%, and 30%, where a larger variance was observed in other porosity groups [Fig. 9(b)]. In high-porosity groups, the yield strain and stress of a majority of samples both varied in a small range of less than 10% despite porosity [Figs. 9(c and d)], and the fracture energy reached a maximum at 9% porosity [see Fig. 9(e); for sample consisting of pure matrix, the fracture energy was 1.75 J/m²]. From a practical point of view, the desired porosity of 9%–12% seems to be the optimal range for balancing material weight and mechanical behavior.

Stochastic Micromechanical Damage Model for Low-Porosity Samples

As shown in Fig. 8, the computed stress–strain curves exhibit some level of nonlinearity, which tends to increase upon increasing porosity. This arises from the fact that increasing stochastic combinations of voids tend to promote ductile events. In this paper, to describe and predict the stress–strain response of porous materials under tension, a stochastic micromechanical damage model was adopted.

Because the simulation results obtained for low porosities (3%-15%) show a nearly perfect elastic response before the peak stress is reached, it is reasonable to assume $f=\infty$. This means that the ensemble that captures the plastic response would perform as a rigid loading bar, where only the elastic response is captured in a microelement. The corresponding constitutive equation of the low porosity group then becomes

$$\sigma = E[\sigma] = (1 - \mu)E(\varepsilon)\varepsilon \tag{18}$$

The mean stress–strain curve in each porosity group was chosen to calibrate the parameters of this model. The modulus was directly computed from the initial slope of the mean stress–strain curves, and the values of the damage variables were determined by fitting the numerical data. Table 2 summarizes the determined parameters (λ and δ) in the distribution function of damage. As shown in Fig. 10, the fitted curves were in good agreement with the numerical results. We obtained a coefficient of determination R^2 greater than 0.983, which indicates that the proposed method was indeed able to capture the average stress–strain response of samples belonging to the low-porosity group.

Stochastic Micromechanical Damage Model for High-Porosity Samples

For higher porosities (18%–30%), the prepeak plastic response was captured by a plastic element with yield threshold f and stiffness αE . The randomly generated fracture strain was assumed to be identical in the two springs—so there was no infinite plastic flow because the spring with modulus E_s broke first (details will be discussed later). Building on Eq. (18), the stress–strain relationship in high porosity samples can be readily obtained as

$$\sigma = \begin{cases} (1 - \mu)E_s \varepsilon & \sigma < f \\ \frac{1}{\alpha + 1}(1 - \mu)(\alpha E_s \varepsilon + f) & \sigma \ge f \end{cases}$$
(19)

Similarly, as in the section "Stochastic Micromechanical Damage Model for Low-Porosity Samples," we focus on the mean stress-strain curve in each porosity group for further examination. Values of the damage variables were determined by fitting the micromechanics model to the numerical data. The modulus was directly computed from the initial slope in the mean curves

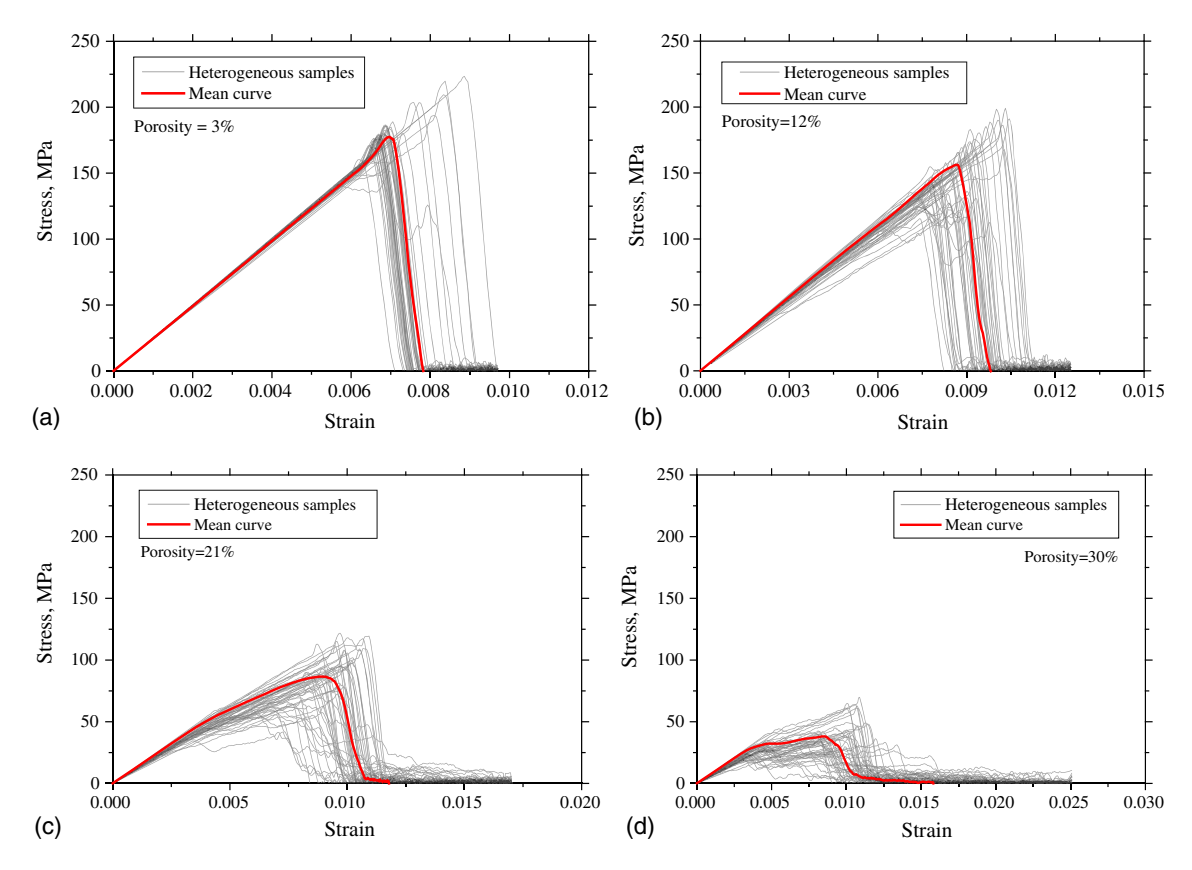


Fig. 8. Stress–strain curves obtained from peridynamic simulations for different representative porosity groups. For each case, the mean curve is shown: (a) porosity = 3%; (b) porosity = 12%; (c) porosity = 21%; and (d) porosity = 30%.

(in the elastic range), and f and α were obtained from the mean curves at the yielding stage. Table 3 summarizes the obtained parameters. As shown in Fig. 11, the fitted curves were in good agreement with the numerical results. We obtained a coefficient of determination R^2 value greater than 0.983, which indicates that the proposed method can match the stress–strain response of samples belonging to the high-porosity group.

As mentioned previously, in micromechanical models, a spring with modulus E_s will break first to prevent any infinite plastic flow. This statement is axiomatic when $\alpha \ge 1$, whereas if $\alpha < 1$, the statement is also valid in this study. To demonstrate this, when the porosity is 27% and $\alpha = 0.75$, the critical stress σ_c under which the two springs reach the same strain can be calculated as

$$\frac{\sigma_c}{E_s} = \frac{\sigma_c - f}{\alpha E_s} \tag{20}$$

This gives $\sigma_c = 139.6$ MPa—which means that the spring with modulus αE breaks first only when the stress exceeds 139.6 MPa. However, this does not happen for such a high porosity because the peak stress is only 52.3 MPa. Similarly, for a porosity of 30%, the critical stress is 56.2 MPa, which is also higher than the peak stress obtained in numerical results for samples with a porosity of 30%.

Influence of the Void Structure on the Model

As shown in Fig. 8, the porous samples showed significant variance in their stress–strain responses, wherein the level of variability increased upon increasing porosity. This phenomenon is attributed to the void structure, which is usually characterized by the shape,

type, and size of the pores (Amran et al. 2015; Chung et al. 2017; Hilal et al. 2015; Nambiar and Ramamurthy 2007; Yu et al. 2011). For low porosities, the average elastic modulus is nearly constant (i.e., not affected by the pore structure), due to the limited number of voids. However, under higher porosities, such as 21%–30%, the void structure exhibits a significant influence on the elastic modulus, yield stress, and fracture energy. Based on this observation, it is crucial to investigate the influence of the void structure on those mechanical properties. In the following section, we propose some parameters to quantify some relevant features of the void structure. We conducted a sensitivity analysis to quantify the influence of those features on the mechanical properties.

Sensitivity Analysis

We first focused on the connectivity of the voids. The voids exhibited three types of contact between each other, which are shown in Fig. 12: (1) "merged voids," wherein two or more void cells share a common edge; (2) "border voids," wherein cells share a common vertex; and (3) "insular voids," wherein a given cell is fully isolated from the others.

For simplicity, the parameters characterizing the void structure were chosen as (1) the average circularity of the voids ($S_{\rm void}$), (2) the volume of the merged voids ($V_{\rm void}$), and (3) the maximum volume of a single merged void ($M_{\rm void}$). Circularity is used to evaluate how closely the shape of an object approaches that of a perfect circle and is defined as the ratio of the surface area of a given void to the surface area of the circle with the same perimeter. A circularity value that is close to zero means the void shape is more irregular and easily leads to a higher local stress concentration. To determine how the different factors of void structure affect

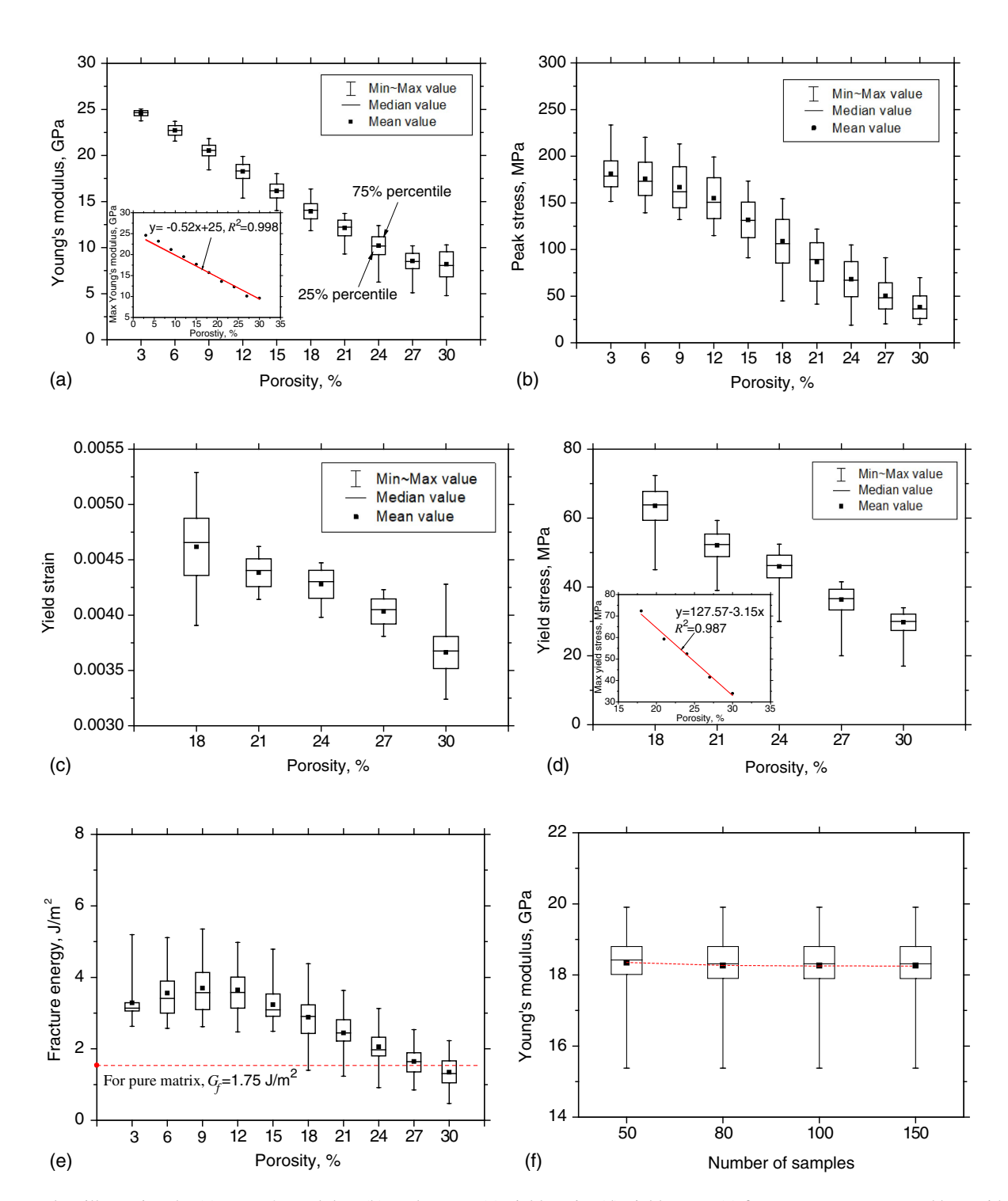


Fig. 9. Box plots illustrating the (a) Young's modulus; (b) peak stress; (c) yield strain; (d) yield stress; (e) fracture energy computed by peridynamics as a function of porosity; and (f) box plot of Young's modulus values for a porosity of 12% based on the statistical analysis of a group of 50, 80, 100, and 150 samples.

Table 2. Parameters used in the present analytical model to describe the stress–strain curve of low-porosity samples

Porosity (%)	E_s (GPa)	λ	δ	R^2
3	24.7	-4.9069	0.02675	0.997
6	22.5	-4.8047	0.02266	0.988
9	20.8	-4.7483	0.02573	0.983
12	18.4	-4.6918	0.02752	0.992
15	15.8	-4.6516	0.03501	0.998

the mechanical index, we conducted a sensitivity analysis based on orthogonal experiments. Such a combined method has been widely used as an effective way to explore and rank the key factors among different variables when data are limited (Chen et al. 2016; Sun et al. 2014).

The range method is commonly used in sensitivity analyses (Frey and Patil 2002). The influence of a parameter is evaluated by R_j , based on Eq. (21)

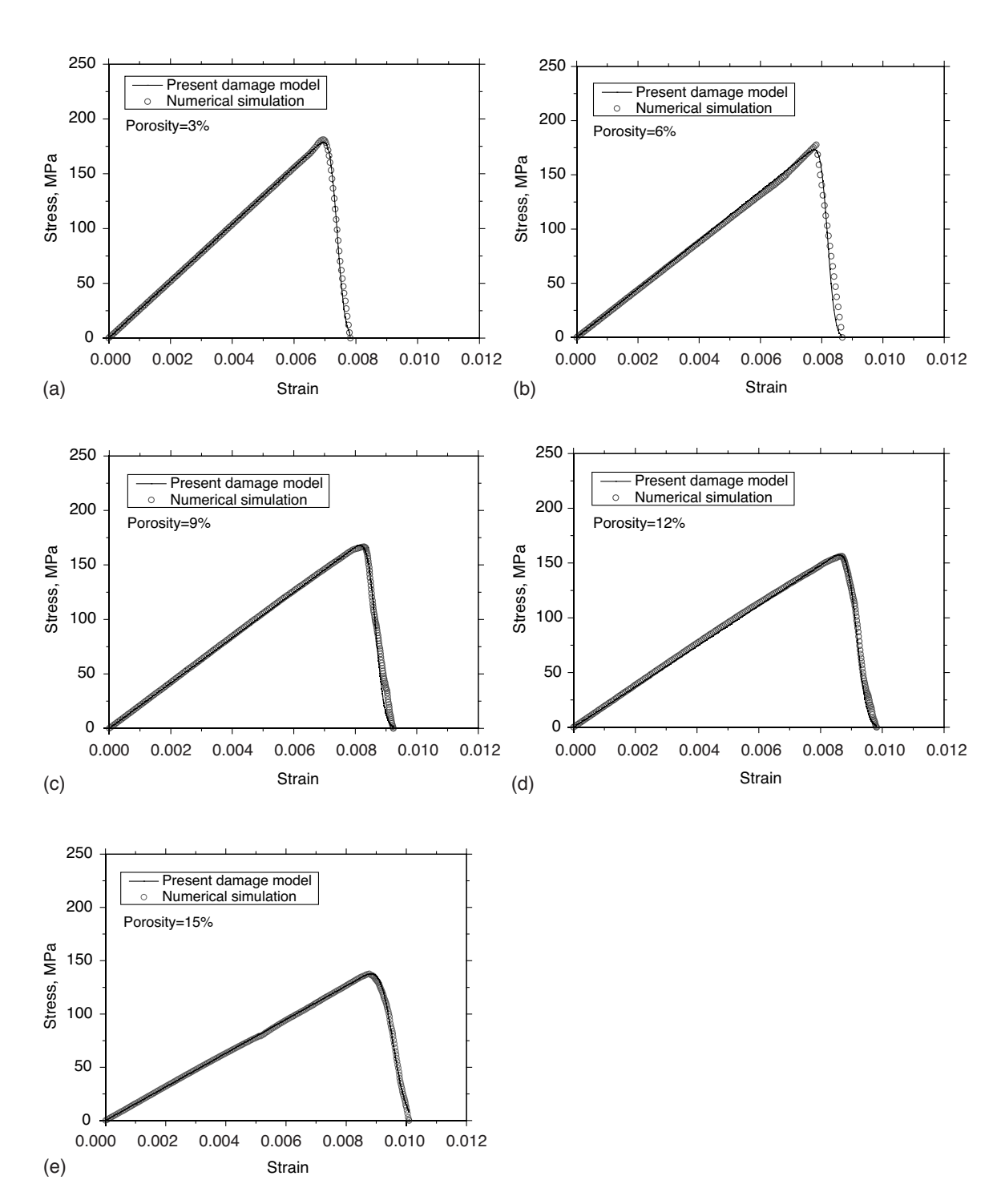


Fig. 10. Stress–strain curves predicted by the present analytical model for different average porosity (for low-porosity samples). The results are compared the average stress–strain curves obtained from the peridynamic simulations: (a) porosity = 3%; (b) porosity = 6%; (c) porosity = 9%; (d) porosity = 12%; and (e) porosity = 15%.

Table 3. Parameters used in the present analytical model to describe the stress–strain curve of high-porosity samples

Porosity (%)	E_s (GPa)	f (MPa)	α	λ	δ	R^2
18	14.2	65.3	4	-4.6329	0.04806	0.999
21	12.3	54.2	2	-4.6097	0.05607	0.999
24	10.8	45.5	1	-4.6283	0.05073	0.993
27	8.4	34.9	0.75	-4.5818	0.07504	0.984
30	7.8	28.1	0.5	-4.6176	0.08502	0.983

$$R_{j} = \max[k_{j1}, k_{j2}, \cdots] - \min[k_{j1}, k_{j2}, \cdots]$$
 (21)

where k_{ji} = sum of test results of certain influence factor under the same level j_i among different test samples. Larger R_j values denote more influential parameters.

An orthogonal experiment table (Table 4) was designed to comprehensively estimate the influence. Three influential factors were considered: void shape $(S_{\rm void})$, void type $(V_{\rm void})$, and

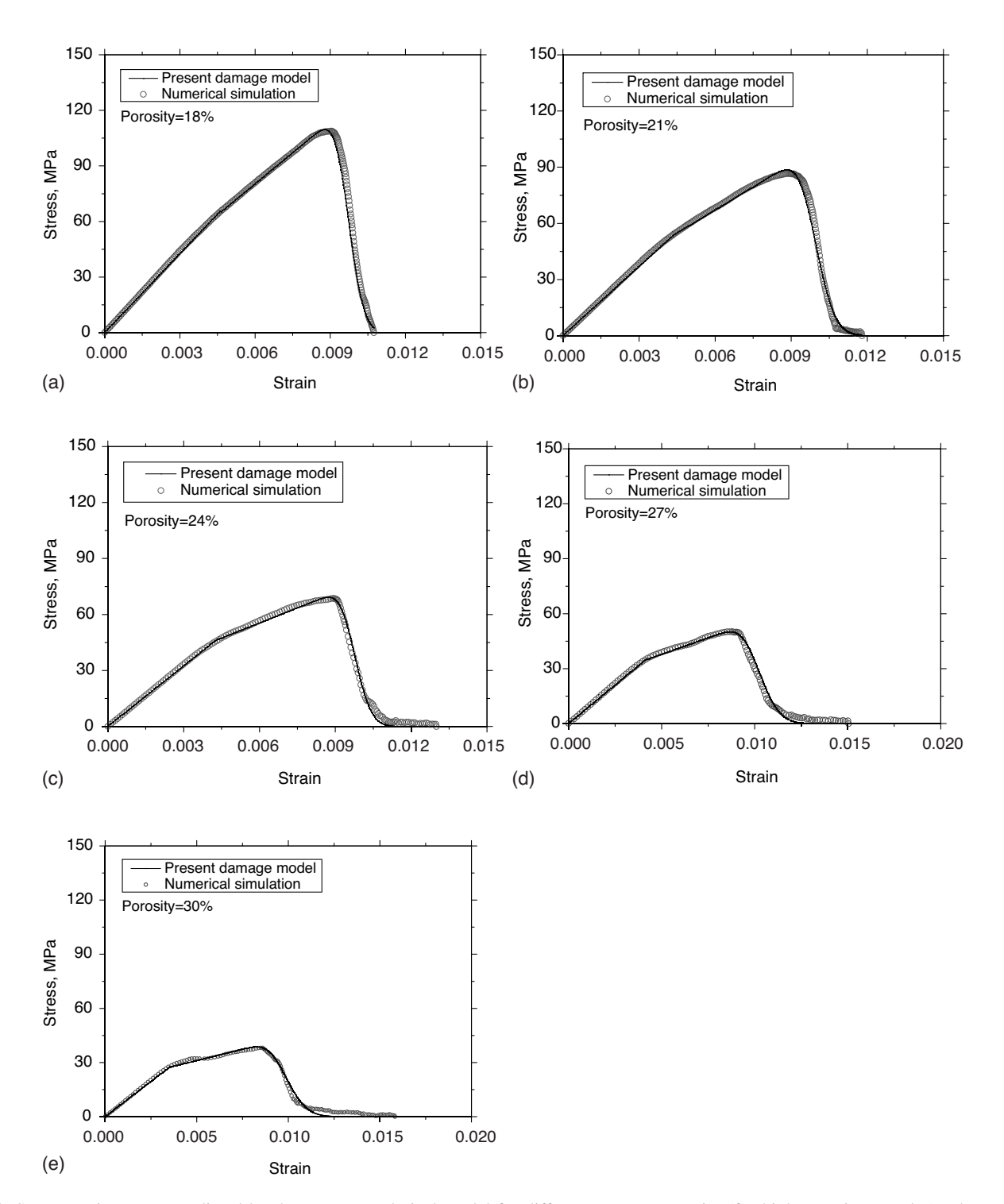


Fig. 11. Stress–strain curves predicted by the present analytical model for different average porosity (for high-porosity samples). The results are compared the average stress–strain curves obtained from the peridynamic simulations: (a) porosity = 18%; (b) porosity = 21%; (c) porosity = 24%; (d) porosity = 27%; and (e) porosity = 30%.

void size $(M_{\rm void})$. Because the values of these influence factors in different porosity groups are inevitably different, $V_{\rm void}$ and $M_{\rm void}$ were normalized according to the total number of void cells in each group. For simply comparing the samples among different porosity groups, each influence factor was divided into three levels labeled as A, B, and C—wherein, in this order, levels A, B, and C indicated that the variation of certain influence factors had a growing negative impact on the mechanical behavior of the porous materials. Specifically, 1,000 samples in different porosity

groups were analyzed. Each A, B, and C level consisted of 20% of the data to prevent errors caused by outliers. For instance, in test sample 6, the $S_{\rm void}$ value was selected from the 40% to 60% percentile of data in descending arrangement of value, $V_{\rm void}$ was selected from the 0% to 20% percentile of data in descending arrangement of value, and $M_{\rm void}$ was selected from the 80% to 100% percentile of data in descending arrangement of value. The data in the bracket of Table 4 indicate associated average values (if more than one sample met the requirements).

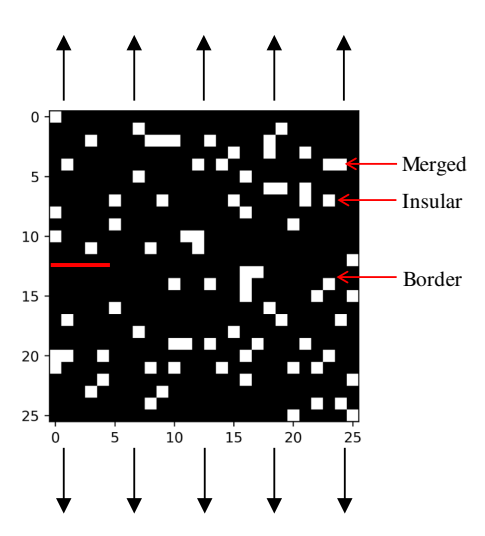


Fig. 12. Schematic illustrating the three types of voids that are defined herein based on their connectivity.

Table 4. Orthogonal experimental factors design and calculation

Test sample	$S_{ m void}$	$V_{ m void}$	$M_{ m void}$	Normalized fracture energy	Normalized modulus
1	A(0.609)	A(0.812)	A(0.097)	0.696	0.873
2	A(0.605)	B(0.861)	B(0.161)	0.374	0.790
3	A(0.605)	C(0.925)	C(0.320)	0.465	0.780
4	B(0.581)	A(0.789)	B(0.145)	0.533	0.766
5	B(0.583)	B(0.869)	C(0.287)	0.459	0.781
6	B(0.588)	C(0.917)	A(0.078)	0.619	0.886
7	C(0.554)	A(0.818)	C(0.288)	0.388	0.674
8	C(0.556)	B(0.872)	A(0.100)	0.668	0.816
9	C(0.555)	C(0.906)	B(0.151)	0.532	0.725

Table 5. Results of the range analysis

Factor	$S_{ m void}$	$V_{ m void}$	$M_{ m void}$
	Fracture	energy	
K_A	1.535	1.617	1.983
K_B	1.611	1.501	1.439
K_C	1.588	1.616	1.312
R_j	0.076	0.116	0.155
	Mod	lulus	
K_A	2.443	2.313	2.575
K_B	2.433	2.387	2.281
K_C	2.215	2.391	2.235
R_j	0.228	0.078	0.155

Fig. 9(c) indicates that, in most samples, the yield strain only slightly fluctuated around its mean value. Here, for convenience, the yield strain is represented by its mean value, whereas the variance of the yield stress can be described by the variance of modulus. The mechanical properties fracture energy and modulus are presented in the range analysis.

Table 5 shows the results of the range analysis. The value of R_j reflects the proportional relation of the three parameters. As a result, the weight coefficients of $S_{\rm void}$, $V_{\rm void}$, and $M_{\rm void}$ for modulus were $W(S_{\rm void})$: $W(V_{\rm void})$: $W(M_{\rm void}) = 0.49$: -0.17: -0.34, respectively, whereas the weight coefficients against $S_{\rm void}$, $V_{\rm void}$, and $M_{\rm void}$ for fracture energy were 0.22:-0.33: -0.45, respectively.

The weight coefficients against $V_{\rm void}$ and $M_{\rm void}$ were negative because increasing the merged-type void and maximum void size has a negative influence on the modulus and fracture energy of porous materials. Accordingly, the influence of the internal structure on the modulus and fracture energy can be simply considered based on the following equation:

$$E^* = \eta_E E^{\text{Bc}} \tag{22a}$$

$$G_f^* = \eta_G G_f^{\text{Bc}} \tag{22b}$$

$$\begin{split} \eta_E &= 1 + f_E \left[\frac{S_{\text{void}}^* - S_{\text{void}}^{\text{Bc}}}{S_{\text{void}}^{\text{Bc}}} \cdot W(S_{\text{void}}^E) + \frac{V_{\text{void}}^* - V_{\text{void}}^{\text{Bc}}}{V_{\text{void}}^{\text{Bc}}} \cdot W(V_{\text{void}}^E) \right. \\ &\left. + \frac{M_{\text{void}}^* - M_{\text{void}}^{\text{Bc}}}{M_{\text{void}}^{\text{Bc}}} \cdot W(M_{\text{void}}^E) \right] \end{split} \tag{22c}$$

$$\eta_G = 1 + f_G \left[\frac{S_{\text{void}}^* - S_{\text{void}}^{\text{Bc}}}{S_{\text{void}}^{\text{Bc}}} \cdot W(S_{\text{void}}^G) + \frac{V_{\text{void}}^* - V_{\text{void}}^{\text{Bc}}}{V_{\text{void}}^{\text{Bc}}} \cdot W(V_{\text{void}}^G) \right]$$

$$+ \frac{M_{\text{void}}^* - M_{\text{void}}^{\text{Bc}}}{M_{\text{void}}^{\text{Bc}}} \cdot W(M_{\text{void}}^G) \right]$$
(22*d*)

where $\eta=$ modified factor that considers the influence of the internal structure; the superscripts * and Bc = targeted sample and baseline cases, respectively; the superscripts E and G = modulus and fracture energy; and f_E and f_G = impact of void structure on the modulus and fracture energy, respectively. The modified factor is a sum of the different percentages of the influence parameters obtained by multiplying their corresponding weight coefficients.

Based on the previous knowledge, the prediction of the stressstrain curves associated with heterogeneous samples is established in the two following sections, that is, for low-porosity and highporosity groups.

Low-Porosity Samples

As shown in Fig. 8(a), for samples with low porosity (3%, 6%, and 9%), the void structure has a significant influence on fracture energy, whereas the modulus is largely unaffected. This is consistent with classical fracture mechanics relationships (Freund 1990). Combining Eqs. (17) and (18) yields $G_f = c \int \sigma d\varepsilon = c \int (1-\mu)E(\varepsilon)d\varepsilon$, which yields $G_f \propto \sum (1-\mu)$. Recalling that μ denotes the expectation of damage, and the damage of porous materials is assumed to follow a lognormal distribution $\ln(\varepsilon) \sim N(\lambda, \delta^2)$, the fracture energy G_f can be described by a function of λ and δ . Accordingly, the stress–strain curve in the low-porosity groups can be described by the distribution variables λ and δ and modulus E_s . The procedure of prediction is summarized as:

- 1. In a given porosity group, calculate the void structure parameters of $S_{\rm void}$, $V_{\rm void}$ and $M_{\rm void}$ for all samples,
- 2. Take one sample as a baseline, so that the modulus E_s of the sample and individual modulus of samples in this porosity group are known. Fit the stress–strain curve with the method described in the section "Stochastic Micromechanical Damage Model for Low-Porosity Samples" to obtain the distribution variables λ and δ , and then find the relationship between fracture energy and the given variables λ and δ , denoted by

$$G_n = f((1+\theta)\lambda, (1+\theta)\delta) \tag{23}$$

3. Consider the fracture energy of the baseline sample as unit 1 and calculate the fracture energy of heterogeneous samples by Eqs. (22b) and (22d), and

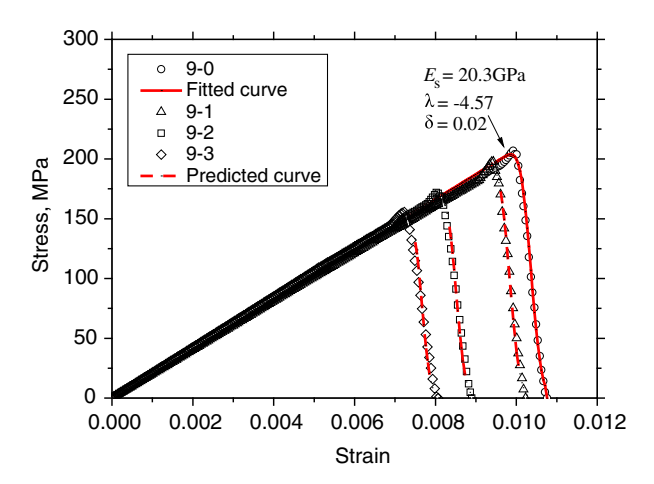


Fig. 13. Stress–strain curves for samples showing the same porosity of 9% but different void structures. The curve associated with sample 9-0 is fitted by present damage model with the parameters $E_s = 20.3$ GPa, $\lambda = -4.57$, and $\delta = 0.02$. In turn, the curves associated with samples 9-1, 9-2, and 9-3 are predicted using Eq. (22).

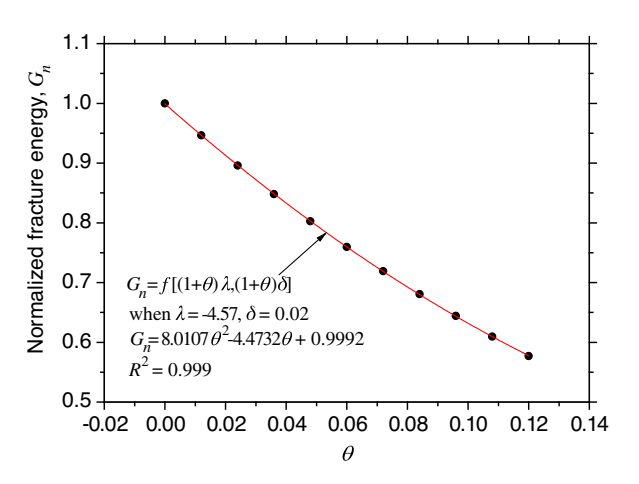


Fig. 14. Normalized fracture energy G_n as a function of θ . When $\lambda = -4.57$ and $\delta = 0.02$, the data can be described by $G_n = 8.0107\theta^2 - 4.4732\theta + 0.9992$.

4. Substitute the fracture energy into Eq. (23). The corresponding value of λ and δ can be obtained so that the stress–strain curve of each sample can be predicted.

As an example, consider the group of 9% porosity. Three samples with different fracture energy values are denoted as 9-1, 9-2, and 9-3 in descending value (Fig. 13). Adopting the method in the section "Stochastic Micromechanical Damage Model for Low-Porosity Samples," the sample with the biggest fracture energy in the porosity group 9% (denoted as 9-0) can be fitted as shown in Fig. 13. The modulus is directly computed from the fitted equation shown in Fig. 9(a). The relationship between the normalized fracture energy G_n , with the distribution variables λ and δ as -4.57 and 0.02, and θ is shown in Fig. 14. This relationship can be perfectly described by a quadratic polynomial. Table 6 shows the value of void structure parameters in each sample. The minimum fracture energy is 50% of the maximum [Fig. 9(e)], so the impact value is $f_G = 0.5$. For 9-1, the fracture energy can be calculated as in Eq. (24). Accordingly, the corresponding θ can be obtained (Table 6)

Table 6. Void structure parameters for the 9% group of porosity

Sample	$egin{array}{cccccccccccccccccccccccccccccccccccc$							
9-0	0.667	0.300	0.0667	1.000	0	0.999		
9-1	0.625	0.283	0.0833	0.947	0.0118	0.999		
9-2	0.689	0.417	0.1000	0.827	0.0415	0.999		
9-3	0.681	0.433	0.1167	0.759	0.0625	0.999		

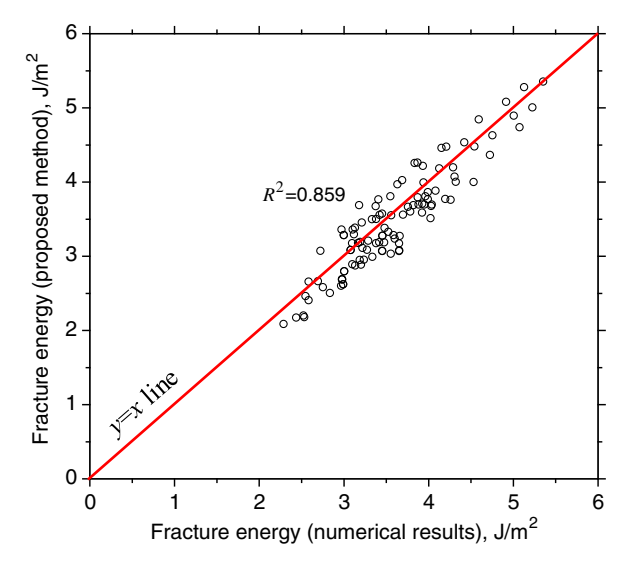


Fig. 15. Comparison between the fracture energy predicted by the present analytical model and simulated values (obtained by peridynamics) for the low-density group. The line (y = x) is indicative of a perfect agreement.

$$1 + 0.5 \left(\frac{0.625 - 0.667}{0.667} \cdot 0.22 + \frac{0.283 - 0.3}{0.3} \cdot (-0.33) + \frac{0.0833 - 0.0667}{0.0667} \cdot (-0.45) \right) = 0.947$$
 (24)

As shown in Fig. 13, the predicted results show good agreement with simulation data. To further validate the proposed method, a comparison of the fracture energy predicted by the present analytical model with simulation results of heterogeneous samples with porosities of 3%, 6%, and 9% is shown in Fig. 15. We observe that the proposed method gives satisfactory results in capturing the mechanical response ($R^2 = 0.859$).

High-Porosity Samples

As shown in Figs. 8(c and d), for samples with high porosity (24%, 27%, and 30%), the void structure has a significant influence on fracture energy G_f , modulus E_s , and yield stress f. By assuming the yield strain ε_y to be represented by a mean value in a certain group, the variance of stress is commensurate with that of the modulus.

For samples with high porosity, the stress–strain curve can be described by the distribution of the variables λ and δ , E_s , and indices of the yield stage α and f. The procedure of prediction is summarized as:

1. In a porosity group, calculate the void structure parameters of $S_{\rm void}$, $V_{\rm void}$ and $M_{\rm void}$ for all samples,

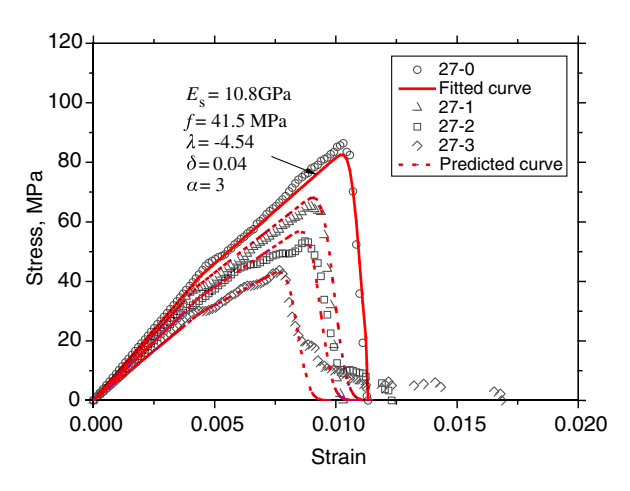


Fig. 16. Stress–strain curves for samples showing the same porosity of 27% but different void structure. The curve associated with sample 27-0 is fitted by the present damage model with the parameters $E_s = 10.8$ GPa, f = 41.5 MPa, $\lambda = -4.54$, $\delta = 0.04$, and $\alpha = 3$. In turn, the curves associated with samples 27-1, 27-2, and 27-3 are predicted using Eq. (22).

2. Take one sample as a baseline so that E_s and f are known. Fit the stress–strain curve with the method in the section "Stochastic Micromechanical Damage Model for High-Porosity Samples" to obtain λ , δ , and α . Then, find the relationship between fracture energy and the given variables based on

$$G_n = h((1+\theta)\lambda, (1+\theta)\delta, \eta_E E_s, \eta_E f, \eta_E \alpha)$$
 (25)

where η_E = modified factor that considers the influence of the internal structure on the modulus, which can be calculated by Eq. (22c),

- Considering the fracture energy of the baseline sample as unit 1, using Eqs. (22a)–(22d) to calculate the fracture energy and modulus of the samples, and
- 4. The values of λ , δ and α can be obtained from Eq. (25), so the stress–strain curve can be predicted.

Taking the group of 27% porosity as an example, three different curves with different modulus values are denoted as 27-1, 27-2, and 27-3 in descending value (Fig. 16). Adopting the method in the section "Stochastic Micromechanical Damage Model for High-Porosity Samples," the sample with the biggest modulus (denoted as 27-0) can be fitted as shown in Fig. 16. The modulus E_s and yield stress f are computed from the fitting equations shown in Figs. 9(a and d), respectively. The relationship between the normalized fracture energy G_n , with the distribution variables λ , δ , and α –4.54, 0.04, and 3, and the fitting variables θ and η_E are shown in Fig. 17. The relationship between distribution variables and fracture energy can be perfectly described by a binary quadratic function.

In the group of density 27%, the impact values for fracture energy f_G and modulus f_E are 0.8 and 0.65. Accordingly, using Eqs. (22a)–(22d), the stress–strain curve of 27-1, 27-2, and 27-3 can be obtained. As shown in Fig. 16 and Table 7, overall, the proposed method properly captured the mechanical response of the samples ($R^2 > 0.968$). To further validate the proposed method, a comparison of the predicted fracture energy and modulus with simulation results of heterogeneous samples with porosities 24%, 27%, and 30% is shown in Fig. 18. We find that the proposed method yields satisfactory results.

As shown in Figs. 13 and 16, the predicted results tend to show good agreement with the simulations in the case of lower porosities.

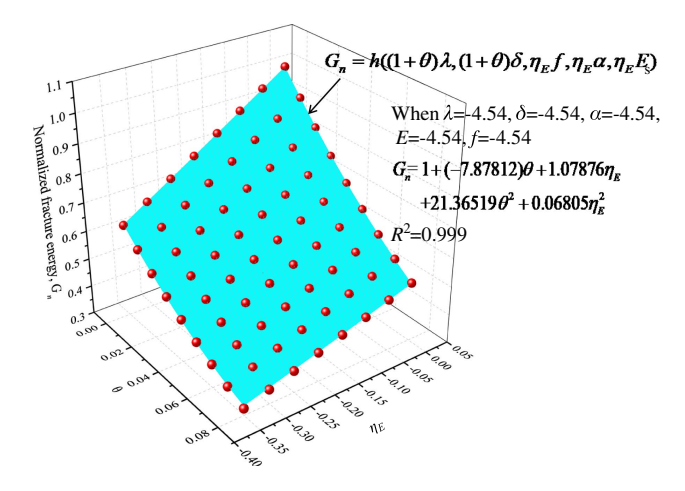


Fig. 17. Normalized fracture energy G_n as a function of the parameters θ and η_E . When $E_s=10.8$ GPa, f=41.5 MPa, $\lambda=-4.54$, $\delta=0.04$, and $\alpha=3$, the data can be described by $G_n=1-7.87812\theta+1.07876\eta_E+21.36519\theta^2+0.06805\eta_E^2$.

Table 7. Void structure parameters for the 27% group of porosity

Sample	$S_{ m void}$	$V_{ m void}$	$M_{ m void}$	Normalized fracture energy, G_n	θ	η_E	R^2
27-0	0.606	0.872	0.122	1.000	0	0	0.999
27-1	0.642	0.822	0.183	0.699	0.014	-0.699	0.996
27-2	0.606	0.925	0.200	0.577	0.028	-0.577	0.992
27-3	0.593	0.872	0.244	0.414	0.064	-0.414	0.968

In the case of higher porosities, the model tends to deviate from the results of the peridynamic simulations in the postpeak range. The prediction is based on the internal void structure and weight coefficients before loading. The void structure evolves in the inelastic range, but the coefficients are not updated to account for this. This is more obvious in the group featuring relatively high porosity because more destructed soft regions tend to form. This will, in turn, cause significant deflection of cracks and result in larger fracture strain after peak stress, whereas those effects cannot be considered in the stochastic damage model.

Conclusions

We proposed a stochastic micromechanical damage model to describe the stress–strain response of porous phases subjected to uniaxial tensile loading. The void structure model was used to predict the heterogeneity of samples with the same porosity. Several conclusions can be drawn from this study:

- Peridynamics offers a powerful tool to simulate the mechanical response of porous materials,
- The proposed micromechanical model properly captures the stress-strain response of porous materials under uniaxial tension while accounting for the heterogeneity of the mechanical response,
- 3. The proposed model offers a good prediction of the average stress-strain curves of porous phases over various ranges of porosity. For heterogeneous samples, the predicted results show good agreement with simulation data in model in the case of low-porosity samples. However, some differences are observed in the case of high-porosity samples. This phenomenon is

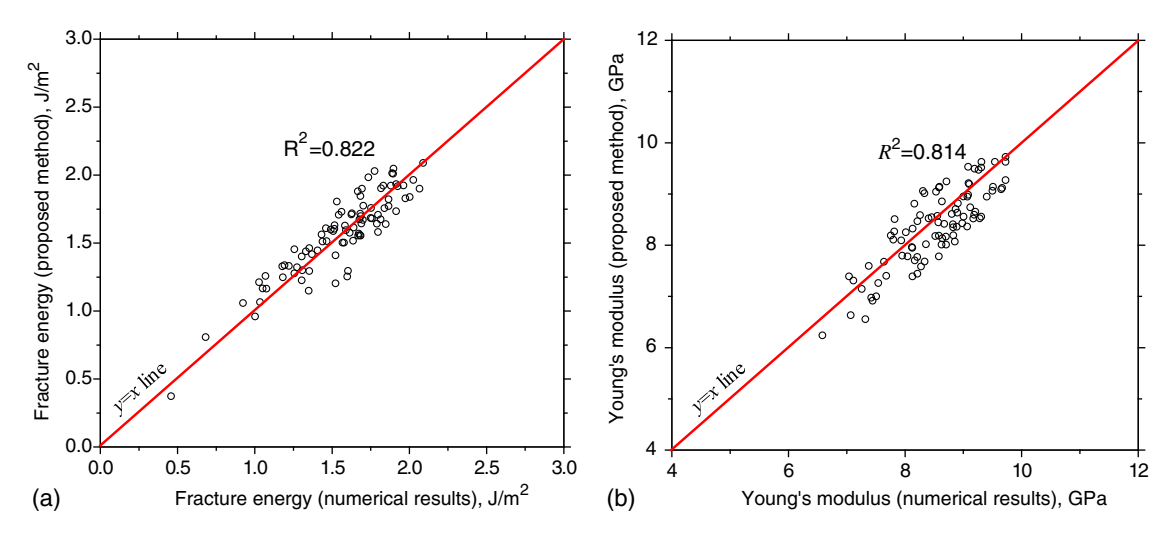


Fig. 18. Comparison between the (a) fracture energy; and (b) Young's modulus predicted by the present analytical model and simulated values (obtained by peridynamics) for the high-density group. The line (y = x) is indicative of perfect agreement.

attributed to a size effect or the fact that the model does not explicitly consider the deflection of cracks, and

4. A sensitivity analysis shows that, at fixed porosity, the maximum pore volume exhibits the strongest influence on fracture energy, whereas the degree of pore circularity has the strongest influence on modulus.

Data Availability Statement

The data that support the findings of this study are available from the corresponding author, Mathieu Bauchy, upon reasonable request.

Acknowledgments

This work was supported by the Division of Civil, Mechanical and Manufacturing Innovation (US) (under Grant Nos. DMREF-1922167, CMMI-1762292, CMMI-1826420, and CMMI-1826050), the National Science Foundation of China (under Grant Nos. 41972272 and 41772281), and the China Scholarship Council (under Grant No. 201906260195).

References

Agwai, A., I. Guven, and E. Madenci. 2011. "Predicting crack propagation with peridynamics: A comparative study." *Int. J. Fract.* 171 (1): 65. https://doi.org/10.1007/s10704-011-9628-4.

Amran, Y. H. M., N. Farzadnia, and A. A. Abang Ali. 2015. "Properties and applications of foamed concrete; a review." *Constr. Build. Mater.* 101 (Dec): 990–1005. https://doi.org/10.1016/j.conbuildmat.2015 .10.112.

Arson, C., and J.-M. Pereira. 2013. "Influence of damage on pore size distribution and permeability of rocks." *Int. J. Numer. Anal. Methods Geomech.* 37 (8): 810–831. https://doi.org/10.1002/nag.1123.

Bauchy, M., H. Laubie, M. J. Abdolhosseini Qomi, C. G. Hoover, F.-J. Ulm, and R. J.-M. Pellenq. 2015. "Fracture toughness of calcium-silicate-hydrate from molecular dynamics simulations." *J. Non-Cryst. Solids* 419 (Jul): 58–64. https://doi.org/10.1016/j.jnoncrysol.2015.03.031.

Bazazzadeh, S., F. Mossaiby, and A. Shojaei. 2020. "An adaptive thermomechanical peridynamic model for fracture analysis in ceramics."

Eng. Fract. Mech. 223 (Jan): 106708. https://doi.org/10.1016/j.engfracmech.2019.106708.

Behzadinasab, M., and J. T. Foster. 2020. "A semi-Lagrangian constitutive correspondence framework for peridynamics." *J. Mech. Phys. Solids* 137 (Apr): 103862. https://doi.org/10.1016/j.jmps.2019.103862.

Chen, Y., H. Yang, and Y. Luo. 2016. "Parameter sensitivity analysis of indirect evaporative cooler (IEC) with condensation from primary air." *Energy Procedia* 88 (Jun): 498–504. https://doi.org/10.1016/j .egypro.2016.06.069.

Chen, Z., S. Niazi, and F. Bobaru. 2019. "A peridynamic model for brittle damage and fracture in porous materials." *Int. J. Rock Mech. Min. Sci.* 122 (Oct): 104059. https://doi.org/10.1016/j.ijrmms.2019.104059.

Chung, S.-Y., C. Lehmann, M. Abd Elrahman, and D. Stephan. 2017. "Pore characteristics and their effects on the material properties of foamed concrete evaluated using micro-CT images and numerical approaches." *Appl. Sci.* 7 (6): 550. https://doi.org/10.3390/app7060550.

Constantinides, G., and F.-J. Ulm. 2004. "The effect of two types of C-S-H on the elasticity of cement-based materials: Results from nanoindentation and micromechanical modeling." *Cem. Concr. Res.* 34 (1): 67–80. https://doi.org/10.1016/S0008-8846(03)00230-8.

Dong, H., P. Gao, and G. Ye. 2017. "Characterization and comparison of capillary pore structures of digital cement pastes." *Mater. Struct.* 50 (2): 154. https://doi.org/10.1617/s11527-017-1023-9.

Fakhimi, A., and E. Alavi Gharahbagh. 2011. "Discrete element analysis of the effect of pore size and pore distribution on the mechanical behavior of rock." *Int. J. Rock Mech. Min. Sci.* 48 (1): 77–85. https://doi.org/10 .1016/j.ijrmms.2010.08.007.

Falliano, D., D. De Domenico, G. Ricciardi, and E. Gugliandolo. 2018. "Experimental investigation on the compressive strength of foamed concrete: Effect of curing conditions, cement type, foaming agent and dry density." Constr. Build. Mater. 165 (Mar): 735–749. https://doi.org/10.1016/j.conbuildmat.2017.12.241.

Faria, R., J. Oliver, and M. Cervera. 1998. "A strain-based plastic viscous-damage model for massive concrete structures." *Int. J. Solids Struct*. 35 (14): 1533–1558. https://doi.org/10.1016/S0020-7683(97)00119-4.

Ferretti, D., E. Michelini, and G. Rosati. 2015. "Cracking in autoclaved aerated concrete: Experimental investigation and XFEM modeling." *Cem. Concr. Res.* 67 (Jan): 156–167. https://doi.org/10.1016/j .cemconres.2014.09.005.

Freund, L. B. 1990. *Dynamic fracture mechanics. Cambridge monographs on mechanics*. Cambridge, UK: Cambridge University Press.

Frey, H. C., and S. R. Patil. 2002. "Identification and review of sensitivity analysis methods." *Risk Anal.* 22 (3): 553–578. https://doi.org/10.1111/0272-4332.00039.

- Hamad, A. J. 2014. "Materials, production, properties and application of aerated lightweight concrete: Review." *Int. J. Mater. Sci. Eng.* 2 (2): 152–157. https://doi.org/10.12720/ijmse.2.2.152-157.
- He, W., Y.-F. Wu, Y. Xu, and T.-T. Fu. 2015. "A thermodynamically consistent nonlocal damage model for concrete materials with unilateral effects." *Comput. Methods Appl. Mech. Eng.* 297 (Dec): 371–391. https://doi.org/10.1016/j.cma.2015.09.010.
- Hilal, A. A., N. H. Thom, and A. R. Dawson. 2015. "On void structure and strength of foamed concrete made without/with additives." *Constr. Build. Mater.* 85 (Jun): 157–164. https://doi.org/10.1016/j.conbuildmat.2015.03.093.
- Hoover, C. G., and F.-J. Ulm. 2015. "Experimental chemo-mechanics of early-age fracture properties of cement paste." *Cem. Concr. Res.* 75 (Sep): 42–52. https://doi.org/10.1016/j.cemconres.2015.04.004.
- Hou, D., D. Li, P. Hua, J. Jiang, and G. Zhang. 2019. "Statistical modelling of compressive strength controlled by porosity and pore size distribution for cementitious materials." *Cem. Concr. Compos.* 96 (Feb): 11– 20. https://doi.org/10.1016/j.cemconcomp.2018.10.012.
- Huang, J., Q. Su, W. Zhao, T. Li, and X. Zhang. 2017. "Experimental study on use of lightweight foam concrete as subgrade bed filler of ballastless track." *Constr. Build. Mater.* 149 (Sep): 911–920. https://doi.org/10 .1016/j.conbuildmat.2017.04.122.
- Huang, Y., Z. Yang, W. Ren, G. Liu, and C. Zhang. 2015. "3D meso-scale fracture modelling and validation of concrete based on in-situ X-ray computed tomography images using damage plasticity model." *Int. J. Solids Struct.* 67–68 (Aug): 340–352. https://doi.org/10.1016/j.ijsolstr.2015.05.002.
- Ju, J. W. 1989. "On energy-based coupled elastoplastic damage theories: Constitutive modeling and computational aspects." *Int. J. Solids Struct*. 25 (7): 803–833. https://doi.org/10.1016/0020-7683(89)90015-2.
- Kandarpa, S., D. J. Kirkner, and B. F. Spencer. 1996. "Stochastic damage model for brittle materials subjected to monotonic loading." J. Eng. Mech. 122 (8): 788–795. https://doi.org/10.1061/(ASCE)0733-9399 (1996)122:8(788).
- Katiyar, A., S. Agrawal, H. Ouchi, P. Seleson, J. T. Foster, and M. M. Sharma. 2020. "A general peridynamics model for multiphase transport of non-Newtonian compressible fluids in porous media." *J. Comput. Phys.* 402 (Feb): 109075. https://doi.org/10.1016/j.jcp.2019.109075.
- Kearsley, E. P., and P. J. Wainwright. 2001. "The effect of high fly ash content on the compressive strength of foamed concrete." Cem. Concr. Res. 31 (1): 105–112. https://doi.org/10.1016/S0008-8846(00)00430-0.
- Kilic, B., A. Agwai, and E. Madenci. 2009. "Peridynamic theory for progressive damage prediction in center-cracked composite laminates." *Compos. Struct.* 90 (2): 141–151. https://doi.org/10.1016/j.compstruct. 2009.02.015.
- Kozlowski, M., M. Kadela, and M. Gwozdz-Lason. 2016. "Numerical fracture analysis of foamed concrete beam using XFEM method." Appl. Mech. Mater. 837 (Jun): 183–186. https://doi.org/10.4028/www .scientific.net/AMM.837.183.
- Kuna, L., J. Mangeri, E. P. Gorzkowski, J. A. Wollmershauser, and S. Nakhmanson. 2020. "Mesoscale modeling of light transmission modulation in ceramics." *Acta Mater.* 193 (Jul): 261–269. https://doi.org/10.1016/j.actamat.2020.03.040.
- Li, J., and X. Ren. 2009. "Stochastic damage model for concrete based on energy equivalent strain." *Int. J. Solids Struct.* 46 (11): 2407–2419. https://doi.org/10.1016/j.ijsolstr.2009.01.024.
- Li, W., and L. Guo. 2020. "A mechanical-diffusive peridynamics coupling model for meso-scale simulation of chloride penetration in concrete under loadings." *Constr. Build. Mater.* 241 (Apr): 118021. https://doi.org/10.1016/j.conbuildmat.2020.118021.
- Liu, D.-M. 1997. "Influence of porosity and pore size on the compressive strength of porous hydroxyapatite ceramic." *Ceram. Int.* 23 (2): 135–139. https://doi.org/10.1016/S0272-8842(96)00009-0.
- Liu, Z., Y. Bie, Z. Cui, and X. Cui. 2020. "Ordinary state-based peridynamics for nonlinear hardening plastic materials' deformation and its fracture process." *Eng. Fract. Mech.* 223 (Jan): 106782. https://doi.org/10.1016/j.engfracmech.2019.106782.
- Lu, Y. L., D. Elsworth, and L. G. Wang. 2013. "Microcrack-based coupled damage and flow modeling of fracturing evolution in permeable brittle

- rocks." Comput. Geotech. 49 (Apr): 226–244. https://doi.org/10.1016/j.compgeo.2012.11.009.
- Madenci, E., and E. Oterkus. 2014. "Peridynamic theory." In *Peridynamic theory and its applications*, edited by E. Madenci and E. Oterkus, 19–43. New York: Springer.
- Maiti, S., K. Rangaswamy, and P. H. Geubelle. 2005. "Mesoscale analysis of dynamic fragmentation of ceramics under tension." *Acta Mater*. 53 (3): 823–834. https://doi.org/10.1016/j.actamat.2004.10.034.
- Mitts, C., S. Naboulsi, C. Przybyla, and E. Madenci. 2020. "Axisymmetric peridynamic analysis of crack deflection in a single strand ceramic matrix composite." *Eng. Fract. Mech.* 235 (Aug): 107074. https://doi.org/10.1016/j.engfracmech.2020.107074.
- Mugahed Amran, Y. H., A. A. Abang Ali, R. S. M. Rashid, F. Hejazi, and N. A. Safiee. 2016. "Structural behavior of axially loaded precast foamed concrete sandwich panels." *Constr. Build. Mater.* 107 (Mar): 307–320. https://doi.org/10.1016/j.conbuildmat.2016.01.020.
- Mydin, M. A. O., and Y. C. Wang. 2012. "Mechanical properties of foamed concrete exposed to high temperatures." *Constr. Build. Mater.* 26 (1): 638–654. https://doi.org/10.1016/j.conbuildmat.2011.06.067.
- Nambiar, E. K. K., and K. Ramamurthy. 2007. "Air-void characterisation of foam concrete." Cem. Concr. Res. 37 (2): 221–230. https://doi.org/10 .1016/j.cemconres.2006.10.009.
- Nguyen, T., A. Ghazlan, A. Kashani, S. Bordas, and T. Ngo. 2018. "3D meso-scale modelling of foamed concrete based on X-ray computed tomography." *Constr. Build. Mater.* 188 (Nov): 583–598. https://doi.org/10.1016/j.conbuildmat.2018.08.085.
- Nguyen, T. T., H. H. Bui, T. D. Ngo, and G. D. Nguyen. 2017. "Experimental and numerical investigation of influence of air-voids on the compressive behaviour of foamed concrete." *Mater. Des.* 130 (Sep): 103–119. https://doi.org/10.1016/j.matdes.2017.05.054.
- Nguyen, T. T., H. H. Bui, T. D. Ngo, G. D. Nguyen, M. U. Kreher, and F. Darve. 2019. "A micromechanical investigation for the effects of pore size and its distribution on geopolymer foam concrete under uniaxial compression." *Eng. Fract. Mech.* 209 (Mar): 228–244. https://doi.org/10.1016/j.engfracmech.2019.01.033.
- Nikonam, M. R., M. D. Pugh, and R. A. L. Drew. 2020. "Pore structure, porosity and compressive strength of highly porous reaction-bonded silicon nitride ceramics with various grain morphologies." *J. Mater. Sci.* 55 (2): 509–523. https://doi.org/10.1007/s10853-019-04078-3.
- Ozaki, S., Y. Aoki, T. Osada, K. Takeo, and W. Nakao. 2018. "Finite element analysis of fracture statistics of ceramics: Effects of grain size and pore size distributions." *J. Am. Ceram. Soc.* 101 (7): 3191–3204. https://doi.org/10.1111/jace.15468.
- Rabczuk, T., and H. Ren. 2017. "A peridynamics formulation for quasistatic fracture and contact in rock." *Eng. Geol.* 225 (Jul): 42–48. https://doi.org/10.1016/j.enggeo.2017.05.001.
- Rabotnov, Y. N. 1969. "Creep rupture." In Applied mechanics: International union of theoretical and applied mechanics, edited by M. Hetényi and W. G. Vincenti, 342–349. Berlin: Springer.
- Rezanezhad, M., S. A. Lajevardi, and S. Karimpouli. 2019. "Effects of pore-crack relative location on crack propagation in porous media using XFEM method." *Theor. Appl. Fract. Mech.* 103 (Oct): 102241. https://doi.org/10.1016/j.tafmec.2019.102241.
- Sadowski, T., and S. Samborski. 2003. "Modeling of porous ceramics response to compressive loading." *J. Am. Ceram. Soc.* 86 (12): 2218–2221. https://doi.org/10.1111/j.1151-2916.2003.tb03637.x.
- Silling, S. A. 2000. "Reformulation of elasticity theory for discontinuities and long-range forces." J. Mech. Phys. Solids 48 (1): 175–209. https:// doi.org/10.1016/S0022-5096(99)00029-0.
- Silling, S. A., and E. Askari. 2005. "A meshfree method based on the peridynamic model of solid mechanics." *Comput. Struct.* 83 (17): 1526–1535. https://doi.org/10.1016/j.compstruc.2004.11.026.
- Silling, S. A., M. Epton, O. Weckner, J. Xu, and E. Askari. 2007. "Peridynamic states and constitutive modeling." *J. Elast.* 88 (2): 151–184. https://doi.org/10.1007/s10659-007-9125-1.
- Sun, P. P., F. Y. Peng, S. Yuan, R. Yan, and Z. Min. 2014. "Sensitivity analysis of tool axis errors in large mill-turn machine tools." *Appl. Mech. Mater.* 487 (Jan): 337–342. https://doi.org/10.4028/www.scientific.net/AMM.487.337.

- Tang, L., N. M. A. Krishnan, J. Berjikian, J. Rivera, M. M. Smedskjaer, J. C. Mauro, W. Zhou, and M. Bauchy. 2018. "Effect of nanoscale phase separation on the fracture behavior of glasses: Toward tough, yet transparent glasses." *Phys. Rev. Mater.* 2 (11): 113602. https://doi.org/10 .1103/PhysRevMaterials.2.113602.
- Tikalsky, P. J., J. Pospisil, and W. MacDonald. 2004. "A method for assessment of the freeze-thaw resistance of preformed foam cellular concrete." Cem. Concr. Res. 34 (5): 889–893. https://doi.org/10.1016/j.cemconres.2003.11.005.
- Unger, J. F., S. Eckardt, and C. Könke. 2007. "Modelling of cohesive crack growth in concrete structures with the extended finite element method." *Comput. Methods Appl. Mech. Eng.* 196 (41): 4087–4100. https://doi.org/10.1016/j.cma.2007.03.023.
- van Mier, J. G. M., and M. R. A. van Vliet. 2002. "Uniaxial tension test for the determination of fracture parameters of concrete: State of the art." *Eng. Fract. Mech.* 69 (2): 235–247. https://doi.org/10.1016/S0013-7944(01)00087-X.
- Wang, X., M. Zhang, and A. P. Jivkov. 2016. "Computational technology for analysis of 3D meso-structure effects on damage and failure of concrete." *Int. J. Solids Struct.* 80 (Feb): 310–333. https://doi.org/10.1016/j .ijsolstr.2015.11.018.
- Wei, S., C. Yiqiang, Z. Yunsheng, and M. R. Jones. 2013. "Characterization and simulation of microstructure and thermal properties of foamed concrete." *Constr. Build. Mater.* 47 (Oct): 1278–1291. https://doi.org/10 .1016/j.conbuildmat.2013.06.027.
- Wu, J. Y., J. Li, and R. Faria. 2006. "An energy release rate-based plastic-damage model for concrete." *Int. J. Solids Struct.* 43 (3): 583–612. https://doi.org/10.1016/j.ijsolstr.2005.05.038.
- Yaghoobi, A., M. G. Chorzepa, and S. S. Kim. 2017. "Mesoscale fracture analysis of multiphase cementitious composites using peridynamics." *Materials* 10 (2): 162. https://doi.org/10.3390/ma10020162.

- Yang, K.-H., K.-H. Lee, J.-K. Song, and M.-H. Gong. 2014. "Properties and sustainability of alkali-activated slag foamed concrete." *J. Cleaner Prod.* 68 (Apr): 226–233. https://doi.org/10.1016/j.jclepro.2013.12.068
- Youssef, M. B., F. Lavergne, K. Sab, K. Miled, and J. Neji. 2018. "Upscaling the elastic stiffness of foam concrete as a three-phase composite material." *Cem. Concr. Res.* 110 (Aug): 13–23. https://doi.org/10.1016/j.cemconres.2018.04.021.
- Yu, X. G., S. S. Luo, Y. N. Gao, H. F. Wang, Y. X. Li, Y. R. Wei, and X. J. Wang. 2011. "Pore structure and microstructure of foam concrete." Adv. Mater. Res. 177 (Dec): 530–532. https://doi.org/10.4028/www.scientific.net/AMR.177.530.
- Yue-Dong, W., and L. Jian. 2011. "Research on foamed cement banking for nonuniform differential settlement in used super highway." In *Proc.*, 2011 Int. Conf. on Electric Technology and Civil Engineering (ICE-TCE). New York: IEEE.
- Zhang, M., and A. P. Jivkov. 2014. "Microstructure-informed modelling of damage evolution in cement paste." *Constr. Build. Mater.* 66 (Sep): 731–742. https://doi.org/10.1016/j.conbuildmat.2014.06.017.
- Zhang, X., W. Huo, J. Liu, Y. Zhang, S. Zhang, and J. Yang. 2020. "3D printing boehmite gel foams into lightweight porous ceramics with hierarchical pore structure." *J. Eur. Ceram. Soc.* 40 (3): 930–934. https://doi.org/10.1016/j.jeurceramsoc.2019.10.032.
- Zhao, X., Q. Li, and S. Xu. 2020. "Contribution of steel fiber on the dynamic tensile properties of hybrid fiber ultra high toughness cementitious composites using Brazilian test." Constr. Build. Mater. 246 (Jun): 118416. https://doi.org/10.1016/j.conbuildmat.2020.118416.
- Zhou, X.-P., Y.-T. Wang, and Y.-D. Shou. 2020. "Hydromechanical bond-based peridynamic model for pressurized and fluid-driven fracturing processes in fissured porous rocks." *Int. J. Rock Mech. Min. Sci.* 132 (Aug): 104383. https://doi.org/10.1016/j.ijrmms.2020.104383.